Cell

Liver exerkine reverses aging- and Alzheimer's-related memory loss via vasculature

Graphical abstract

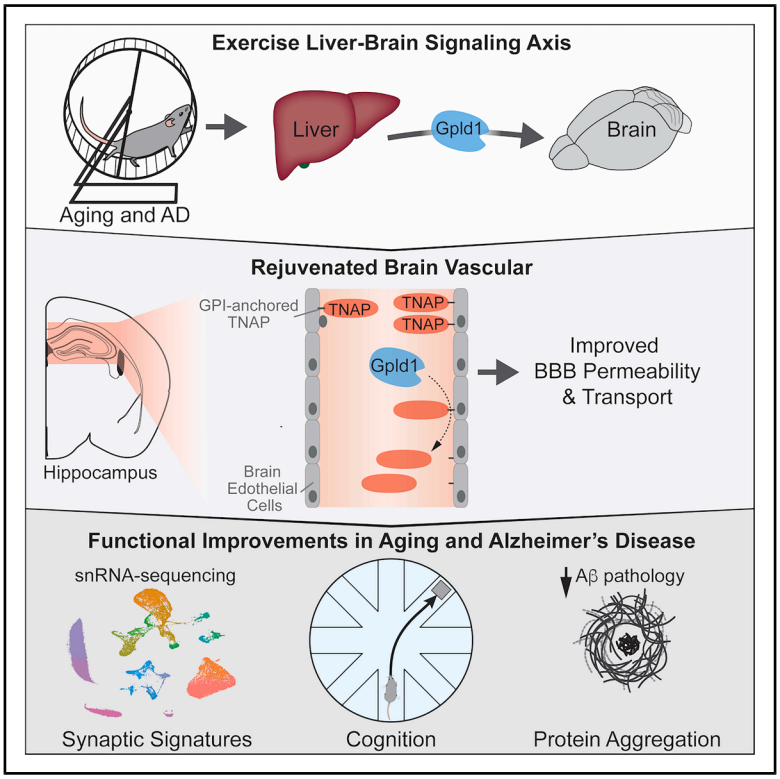

Highlights

- Liver exercise factor GPLD1 targets GPI-anchored proteins on the aged brain vasculature
- GPI-anchored TNAP on brain endothelial cells disrupts the BBB and impairs cognition
- Increased GPLD1 or TNAP inhibition rejuvenates BBB function and cognition in aging
- Increased GPLD1 or TNAP inhibition ameliorates Alzheimer's disease pathology

Authors

Gregor Bieri, Karishma J.B. Pratt, Yasuhiro Fuseya, ..., Andrew C. Yang, Kaitlin B. Casaletto, Saul A. Villeda

Correspondence

gregbieri@gmail.com (G.B.), saul.villeda@ucsf.edu (S.A.V.)

In brief

Liver exercise factor GPLD1 rejuvenates blood-brain barrier integrity and reverses cognitive impairments in aging and Alzheimer's disease models by targeting GPI-anchored proteins on brain endothelial cells.

Bieri et al., 2026, Cell *189*, 1–18
March 5, 2026
https://doi.org/10.1016/j.cell.2026.01.024

CellPress

Please cite this article in press as: Bieri et al., Liver exerkine reverses aging- and Alzheimer's-related memory loss via vasculature, Cell (2026), https://doi.org/10.1016/j.cell.2026.01.024

Cell

CellPress
OPEN ACCESS

Article

Liver exerkine reverses aging- and Alzheimer's-related memory loss via vasculature

Gregor Bieri,[1,*] Karishma J.B. Pratt,[1] Yasuhiro Fuseya,[1] Turan Aghayev,[1] Juliana Sucharov,[1,2] Alana M. Horowitz,[1,2] Amber R. Philp,[1] Karla Fonseca-Valencia,[1,3] Rebecca Chu,[1,2] Mason Phan,[1] Laura Remesal,[1] Shih-Hsiu J. Wang,[4,5] Andrew C. Yang,[6,7] Kaitlin B. Casaletto,[7,8] and Saul A. Villeda[1,3,9,10,11,*]

[1]Department of Anatomy, University of California, San Francisco, San Francisco, CA 94143, USA
[2]Biomedical Sciences Graduate Program, University of California, San Francisco, San Francisco, CA 94143, USA
[3]Pharmaceutical Sciences and Pharmacogenomics Graduate Program, University of California, San Francisco, San Francisco, CA 94143, USA
[4]Department of Pathology, Duke University Medical Center, Durham, NC 27710, USA
[5]Department of Neurology, Duke University Medical Center, Durham, NC 27710, USA
[6]Gladstone Institute of Neurological Disease, San Francisco, CA 94158, USA
[7]Department of Neurology, University of California, San Francisco, San Francisco, CA 94143, USA
[8]Memory and Aging Center, Department of Neurology, University of California, San Francisco, San Francisco, CA 94143, USA
[9]Department of Physical Therapy and Rehabilitation Science, University of California, San Francisco, San Francisco, CA 94143, USA
[10]Bakar Aging Research Institute, University of California, San Francisco, San Francisco, CA 94143, USA
[11]Lead contact
*Correspondence: gregbieri@gmail.com (G.B.), saul.villeda@ucsf.edu (S.A.V.)
https://doi.org/10.1016/j.cell.2026.01.024

SUMMARY

Blood factors transfer the benefits of exercise to the aged brain independent of physical activity. Here, we show that the liver-derived exercise factor (exerkine) glycosylphosphatidylinositol (GPI)-specific phospholipase D1 (GPLD1), a GPI-degrading enzyme, reverses aging- and Alzheimer's-related memory loss by targeting the brain vasculature. GPLD1 has the potential to cleave over 100 putative GPI-anchored proteins, necessitating the identification of downstream targets that mediate cognitive rejuvenation for translational application. We identified GPI-anchored tissue-nonspecific alkaline phosphatase (TNAP) on the brain vasculature as a GPLD1 substrate. Mimicking age-related increases in cerebrovascular TNAP impaired blood-brain transport and cognition in young mice and mitigated GPLD1-induced cognitive benefits in aged mice. Inhibiting TNAP recapitulated the benefits of GPLD1 in old age, restoring youthful hippocampal transcriptional signatures and rescuing cognition. In an Alzheimer's disease model, increasing GPLD1 or inhibiting TNAP ameliorated Aβ pathology and improved cognitive deficits. We thus identify brain vasculature as a mediator of the cognitive benefits of a liver-to-brain exercise axis.

INTRODUCTION

Exercise can reverse broad cellular and molecular hallmarks of brain aging, challenging long-standing views of age-related cognitive dysfunction as a rigid process.[1–3] In the hippocampus—a brain region important for memory and highly sensitive to the detrimental effects of aging—running in aged mice increases regenerative capacity, enhances synaptic plasticity, attenuates neuroinflammation, and boosts associated cognitive function.[2,4–7] In animal models of Alzheimer's disease (AD) pathology, exercise has been shown to improve learning and memory.[8] In humans, increased physical activity is associated with reduced risk of dementia,[9,10] slowed cognitive decline with age,[11] and delayed dementia onset,[10] even in autosomal dominant forms of AD.[12] Unfortunately, its consistent application is often impeded in the elderly by physical and medical limitations.[13–15] Therefore, identifying alternative means to confer the cognitive benefits of exercise without physical activity may provide a unique and unexplored therapeutic approach.

We and others recently demonstrated that systemic administration of blood plasma from exercised to sedentary mice can transfer the benefits of exercise on the aged brain, independent of physical activity.[16–18] We identified glycosylphosphatidylinositol (GPI)-specific phospholipase D1 (GPLD1), a liver-derived GPI-degrading enzyme, as an exercise-induced circulating blood factor (exerkine).[16] While we demonstrated a striking cognitive benefit of GPLD1 administration in aged mice,[16] GPLD1 has the potential to cleave over 100 putative GPI-anchored proteins. Therefore, to pursue the therapeutic potential of liver-derived GPLD1 in brain aging, it is important to identify downstream cellular and molecular targets that mediate cognitive rejuvenation for translational application to dementia-related neurodegenerative disorders, such as AD. Interestingly, increasing systemic GPLD1 improved cognitive function without

Please cite this article in press as: Bieri et al., Liver exerkine reverses aging- and Alzheimer's-related memory loss via vasculature, Cell (2026), https://doi.org/10.1016/j.cell.2026.01.024

readily entering the brain,[16] highlighting yet unidentified peripheral mechanisms of action.

To investigate factors downstream of GPLD1, we used bioinformatics and targeted candidate-based testing to identify GPI-anchored tissue-nonspecific alkaline phosphatase (TNAP) as a GPLD1 substrate on brain vasculature that is strongly upregulated during aging. Mimicking the age-related increase in cerebrovascular TNAP expression impaired blood-brain barrier (BBB) function and cognition in young mice and mitigated GPLD1-induced cognitive benefits in aged mice, whereas inhibiting TNAP activity recapitulated the transcriptional and cognitive effects of GPLD1 administration in aged mice. We found liver GPLD1 increased following exercise in a 5xFAD mouse model of AD pathology, and TNAP was elevated in the brains of older adults and AD individuals compared with healthy young humans. Moreover, increasing liver-derived GPLD1, or inhibiting TNAP activity, reversed AD-related hippocampal transcriptional signatures, ameliorated Aβ pathology, and improved cognitive deficits. These findings indicate that brain vasculature is an important mediator of the restorative cognitive benefits of liver-derived exercise blood factors.

RESULTS

GPI-anchored TNAP is a GPLD1 substrate on the aged hippocampal vasculature

To begin, we first validated increased GPLD1 expression in the liver of aged mice in response to a voluntary exercise intervention compared with sedentary controls (Figures S1A–S1E). We mimicked the exercise-induced increase of GPLD1 in the liver of aged mice using an *in vivo* hydrodynamic tail-vein injection (HDTVI)-mediated overexpression approach. We assessed health metrics and hippocampal-dependent memory using novel object recognition (NOR) and Y-maze behavioral tasks (Figures S1F–S1L). Young control mice were biased toward a novel object and a novel arm relative to a familiar condition during NOR and Y-maze testing, respectively, while aged control mice showed no preference (Figures S1G and S1H). However, age-related cognitive impairments were reversed in GPLD1-treated aged mice (Figures S1G and S1H). To identify potential downstream peripheral cellular and molecular targets mediating these cognitive rejuvenating effects of liver-derived GPLD1, we focused our analysis on candidate GPI-anchored proteins. To begin, we leveraged publicly available single-cell RNA sequencing (scRNA-seq) datasets[19,20] and surveyed cellular expression of 148 putative GPI-anchored proteins across tissues (Figure 1A; Table S1).[19,20] We observed a high concentration of GPI-anchored proteins expressed on endothelial and epithelial cells (Figure 1A), positing vasculature as a potential GPLD1 target at the interface of the blood and brain.

We next analyzed age-related GPI-anchored protein expression changes on brain endothelial cells (BECs) using a publicly available RNA-seq dataset of young and aged mice.[21,22] We identified 11 upregulated and 2 downregulated genes, of which *alkaline phosphatase, biomineralization associated* (*Alpl*) (encoding TNAP) was among the most significantly increased with age (Figures 1A and 1B). While its canonical function is still incompletely understood, TNAP is one of four alkaline phosphatase (AP) isoenzymes whose canonical role is to promote tissue mineralization and vascular calcification.[23–25] It was recently shown that age-related increased cerebrovascular TNAP impairs blood-brain transport, while TNAP inhibition restores youthful blood-brain transport.[26] Consequently, we elected to investigate whether vascular TNAP is a GPI-anchored GPLD1 substrate.

In the hippocampus, we found an age-related increase in TNAP vascular expression and AP activity staining (Figures 1C–1E, S1M, and S1N). Similar increases were observed in additional brain regions (Figures S2A and S2B). Additionally, we observed a decrease in TNAP expression and AP activity in the cerebrovasculature of exercised compared with sedentary aged mice (Figures 1F–1H), while *Alpl* mRNA expression in the hippocampus remained unchanged (Figure S1O).

To investigate the possibility of TNAP being a GPI-anchored GPLD1 substrate, we opted to first leverage an *in vitro* approach. The catalytic activity of GPLD1 is dependent on His133,[27] with His133→Asn (H133N) or His158→Asn (H158N) amino acid substitutions ablating its enzymatic activity, which we validated using a cleavage reporter assay of the known GPLD1 substrate ALPP (Figure S2F).[16,28] We next generated a constitutively expressing TNAP reporter cell line in which cleavage can be assessed by measuring the AP activity of TNAP in the supernatant upon its cleavage and release from the plasma membrane (Figure 1I). TNAP-expressing cells were treated with mouse or human GPLD1, catalytically inactive H133N or H158N GPLD1, or green fluorescent protein (GFP) control (Figures 1I and S2G). We detected a significant increase in TNAP-mediated AP activity in the supernatant from cells treated with mouse GPLD1 or human GPLD1 but not catalytically inactive H133N or H158N GPLD1 or GFP controls (Figures 1J and S2G), establishing TNAP as a direct GPI-anchored GPLD1 substrate.

To investigate whether vascular TNAP is a GPI-anchored GPLD1 substrate *in vivo*, we assessed changes in vascular TNAP expression and AP activity in the hippocampus of aged mice following increased liver-derived GPLD1 (Figure 1K). Aged male mice were given HDTVI with expression constructs encoding GPLD1, catalytically inactive H133N GPLD1, or GFP, and TNAP expression and AP activity were assessed on hippocampal vasculature (Figures 1K–1M). Increased liver-derived GPLD1 resulted in decreased vascular TNAP expression and AP activity staining in the hippocampal vasculature compared with the catalytically inactive H133N GPLD1 or GFP control treatment groups (Figures 1L and 1M). Liver-derived GPLD1 also decreased AP activity staining in additional brain areas surveyed (Figures S2C and S2D). Of note, we observe that GPLD1 treatment does not alter the mRNA expression of *Alpl* in the aged hippocampus (Figure S1P), indicating that the decrease in TNAP protein expression observed in GPLD1-treated aged mice is not due to changes at the mRNA level. Additionally, we orthogonally measured levels of circulating TNAP in blood plasma at baseline and following acute expression of liver-derived GPLD1 in an independent cohort of aged mice and observed an increase in circulating TNAP (Figures S2H and S2I). Given that circulating TNAP by nature must be derived from the plasma membrane protein that was cleaved, increased blood levels following GPLD1 treatment provide further evidence of TNAP cleavage *in vivo*. Collectively, these data indicate that cerebrovascular TNAP is a GPI-anchored GPLD1 substrate.

Please cite this article in press as: Bieri et al., Liver exerkine reverses aging- and Alzheimer's-related memory loss via vasculature, Cell (2026), https://doi.org/10.1016/j.cell.2026.01.024

CellPress
OPEN ACCESS

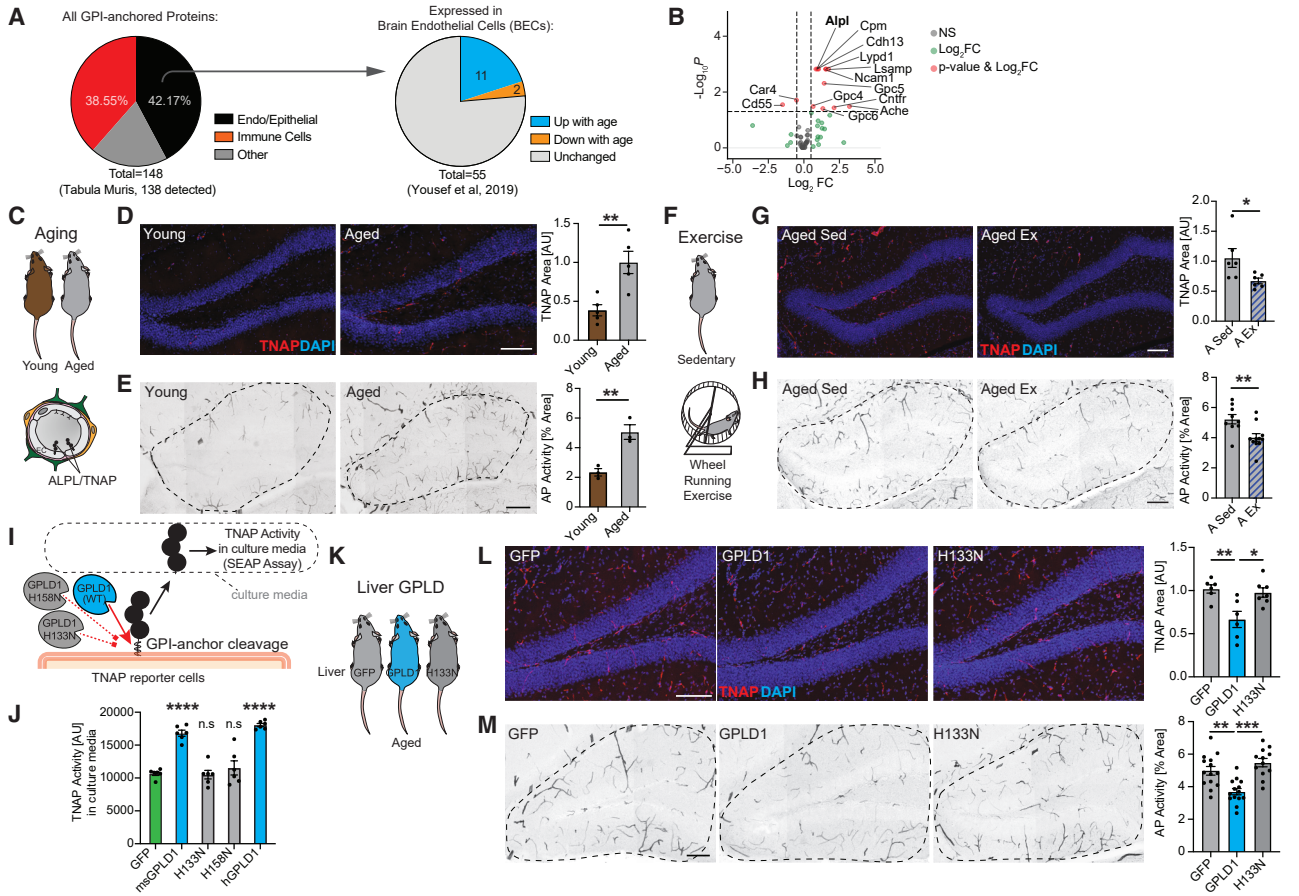

Figure 1. GPI-anchored TNAP is a GPLD1 substrate on the aged hippocampal vasculature

(A) Pie charts of murine GPI-anchored protein expression by major cell categories (left). Differential GPI-anchored protein expression in mouse brain endothelial cells (BECs) (right; adapted from Yousef et al.[19]).

(B) Volcano plot of GPI-anchored proteins in young and aged mouse BECs (adapted from Yousef et al.[19]).

(C) Expression of the potential GPLD1 substrate ALPL/tissue non-specific alkaline phosphatase (TNAP) on BECs.

(D) Representative images and quantification of TNAP labeling (red) in the hippocampal dentate gyrus (DG) region of young (3 months) and aged mice (22–24 months) (n = 4 mice/group).

(E) Representative images and quantifications of endogenous alkaline phosphatase (AP) labeling in the DG (dashed line, stitched overview image) of young and aged mice (n = 3 mice/group).

(F) Aged mice (19–21 months) underwent a 6-week-long voluntary exercise intervention.

(G) Representative images and quantification of TNAP immunostaining in the DG of aged exercised mice (n = 5–6 mice/group).

(H) Representative images and quantifications of endogenous AP labeling in the DG of aged exercised mice (n = 9–11 mice/group).

(I and J) Schematic illustration (I) and quantification (J) of TNAP cleavage and secreted AP (SEAP) assay in the culture media of TNAP reporter cells following treatment with mouse or human GPLD1, catalytically inactive GPLD1 with the histidine H133N (H133N) or histidine H158N (H158N) amino acid substitution, or GFP control (n = 6 wells/condition).

(K) Aged mice (20–22 months) with liver overexpression of GPLD1, H133N, or GFP control using an HDTVI approach.

(L) Representative images and quantification of TNAP immunostaining in DG of aged mice following liver GPLD1, H133N, or GFP overexpression (n = 6–7 mice/group).

(M) Representative images and quantification of endogenous AP labeling in the DG of aged mice following liver GPLD1, H133N, or GFP overexpression (n = 12–14 mice/group).

Data shown as mean ± SEM. Scale bar, 200 μm. Statistical analysis was performed using t test (D, E, G, and H) and ANOVA with Šidák's post hoc test (J, L, and M); $^{*}p < 0.05$, $^{**}p < 0.01$, $^{***}p < 0.001$, $^{****}p < 0.0001$.

See also Figures S1 and S2.

Increasing liver-derived GPLD1 rejuvenates BBB function in the aged hippocampus

Having identified TNAP as a GPLD1 substrate and given the role of increased cerebrovascular TNAP expression in blood-brain transport dysfunction in aging, we next examined the effect of increasing liver-derived GPLD1 on BBB function in the aged hippocampus (Figure 2A). Aged mice were given retro-orbital injections of liver-specific adeno-associated virus (AAV) encoding GPLD1 or catalytically inactive H133N GPLD1 (Figures 2A and S2E). To establish a baseline for age-related changes in BBB

Please cite this article in press as: Bieri et al., Liver exerkine reverses aging- and Alzheimer's-related memory loss via vasculature, Cell (2026), https://doi.org/10.1016/j.cell.2026.01.024

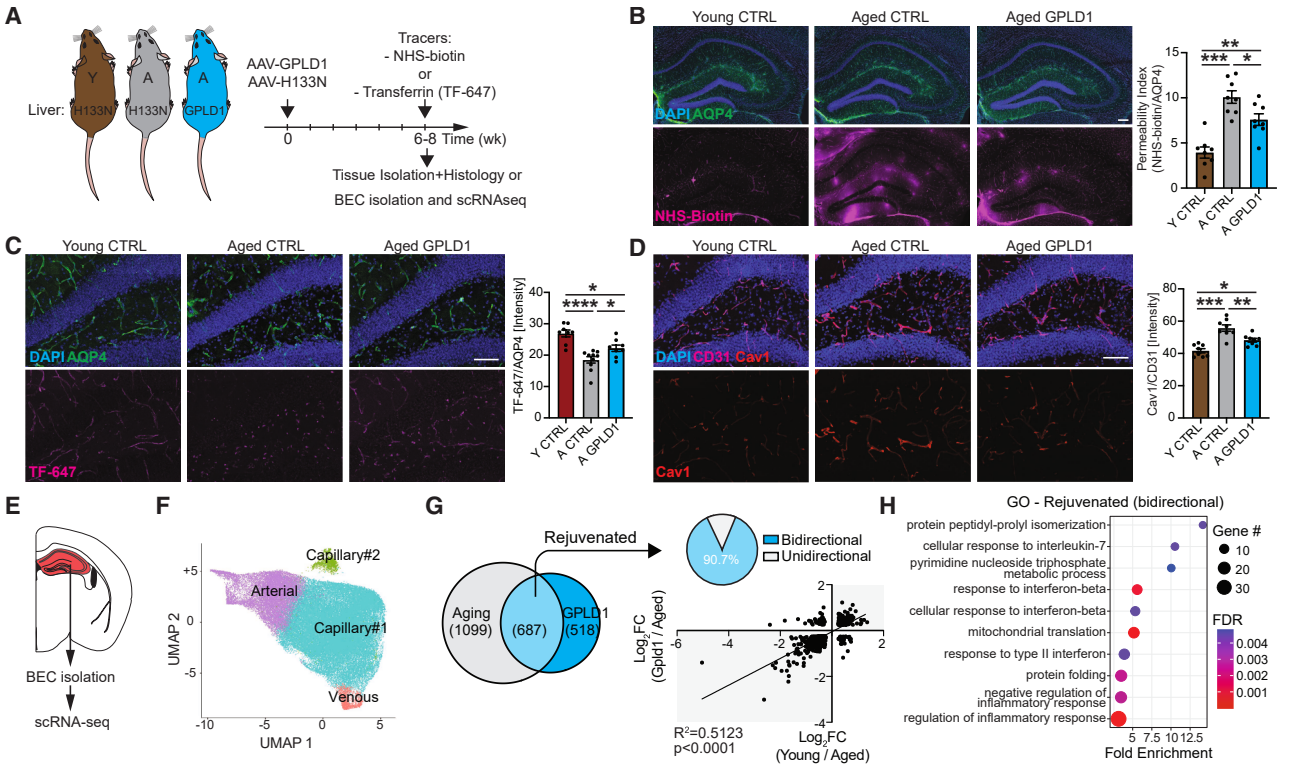

Figure 2. Increasing liver-derived GPLD1 rejuvenates BBB function in the aged hippocampus

(A) Vascular function was analyzed in young (4–5 months) and aged (22–24 months) mice after AAV-mediated liver overexpression of GPLD1 or inactive H133N GPLD1 using NHS-biotin tracer, fluorescently labeled transferrin (TF-647), immunohistochemistry, or scRNA-seq of BECs.

(B) Representative images and quantification of NHS-biotin leakage from hippocampal blood vessels.

(C) Representative images and quantification of TF-647 uptake by hippocampal blood vessels.

(D) Representative images and quantification of Caveolin-1 (Cav1) immunostaining in hippocampal blood vessels (n = 7–8 mice/group).

(E) Single-cell RNA-sequencing (scRNA-seq) analysis of hippocampal BECs from young and aged mice treated with GPLD1 or H133N control.

(F) Uniform manifold approximation and projection (UMAP) of BEC scRNA-seq analysis.

(G) Venn diagram (left) of the number of differentially expressed genes (DEGs) for the aging comparison (gray, young versus aged control) and GPLD1 comparison (blue, aged GPLD1 versus aged control). Pie chart of 687 overlapping DEGs between aging and GPLD1 comparisons (top) separated by unidirectional versus bidirectional changes. Overlapping bidirectional DEGs between the aging and GPLD1 comparisons are referred to as the rejuvenated signature. Scatterplot (bottom) of overlapping genes between the aging (x axis) and GPLD1 comparisons (y axis).

(H) Top Gene Ontology (GO) terms of biological processes associated with rejuvenated DEGs.

Data shown as mean ± SEM. Scale bar, 100 μm. Statistical analysis was performed using ANOVA with Šidák's post hoc test (B–D) and linear regression (G); $^{*}p < 0.05$, $^{**}p < 0.01$, $^{***}p < 0.001$, $^{****}p < 0.0001$.

See also Figure S3.

function,[26,29,30] an additional control group of young mice given retro-orbital injections with liver-specific AAV encoding H133N GPLD1 was included (Figure 2A). We assessed GPLD1 expression across several highly vascularized tissues and observed a selective increase only in the liver, further validating the specificity of the AAV-delivery approach (Figure S2E).

To evaluate BBB permeability, a subset of animals was systemically administered the small molecule tracer N-hydroxysuccinimide (NHS)-biotin (Figure 2B). Consistent with age-related dysfunctional blood-brain transport,[30] we detected numerous hotspots of NHS-biotin leakage outside of blood vessels in the hippocampi of aged compared with young control animals (Figure 2B). However, increased liver-derived GPLD1 resulted in significantly reduced NHS-biotin leakage from blood vessels broadly across the aged hippocampus (Figure 2B).

In the aging cerebrovasculature, a shift from receptor-mediated transport to caveolar transcytosis has also been reported.[26] To assess receptor-mediated transport, a subset of animals was systemically administered with fluorescently labeled canonical ligand transferrin (TF-647) (Figures 2A and 2C). An age-related decrease in TF-647 transport was observed in the hippocampus of aged compared with young control animals; however, this decrease was in part blunted in the aged GPLD1 treatment group (Figure 2C). Next, we examined ligand-non-specific caveolae by measuring expression of Caveolin-1 (Cav1), a structural protein of caveolae that increases with age.[26,29] While increased Cav1 expression was detected on blood vessels from the hippocampi of aged compared with young control animals, Cav1 expression was significantly reduced in aged animals with increased liver-derived GPLD1 (Figure 2D). Collectively, these data demonstrate

Please cite this article in press as: Bieri et al., Liver exerkine reverses aging- and Alzheimer's-related memory loss via vasculature, Cell (2026), https://doi.org/10.1016/j.cell.2026.01.024

that increased liver-derived GPLD1 improves BBB function in the aged hippocampus.

To gain mechanistic insight into the molecular changes induced in BECs by increased liver-derived GPLD1, we used scRNA-seq. BECs were isolated from hippocampi of aged mice expressing liver-derived GPLD1 or H133N GPLD1, or young mice expressing liver-derived H133N GPLD1 (Figure 2E). Arterial, capillary, and venous clusters were identified (Figures 2F and S3A–S3E). We detected prominent transcriptional changes in BECs due to aging (Figure 2G), of which over 38% were restored toward a youthful profile following increased liver-derived GPLD1 (Figure 2G). Subsequently, we focused our analysis on differentially expressed genes (DEGs) that change in aging but are rescued following GPLD1 treatment (Figures 1G and S3F–S3H). Gene Ontology (GO) analysis of DEGs identified biological processes related to inflammatory processes, energy metabolism, and proteostasis (Figure 2H). These single-cell transcriptomics data indicate that increasing liver-derived GPLD1, in part, restores more youthful transcriptional signatures in BECs from the aged hippocampus.

Mimicking the age-related increase in cerebrovascular TNAP disrupts hippocampal BBB function and impairs cognition

While increased TNAP expression on the aging cerebrovasculature has been shown to impair proper blood-brain transport to the aged brain,[26] its impact on cognition has yet to be explored. Therefore, we assessed the functional consequence of mimicking an age-related increase in cerebrovascular TNAP expression on BBB function and hippocampal-dependent memory in young mice using a cell-type-specific, viral-mediated overexpression approach.[31] Young mice were given retro-orbital injections of BEC-specific AAV encoding TNAP or mRuby2 (Ruby) as a control (Figures 3A and S4A–S4C). Increased TNAP expression and AP activity were confirmed on hippocampal vasculature following AAV-TNAP injection (Figures 3B and S4C–S4E).

BBB function was assessed using NHS-biotin tracer and fluorescently labeled transferrin (Figure 3A). Young animals overexpressing cerebrovascular TNAP exhibited increased NHS-biotin leakage from blood vessels and decreased TF-647 transport in the hippocampus compared with young control animals (Figures 3C and 3D). Concurrently, we observed increased Cav1 expression on blood vessels following TNAP overexpression (Figure 3E).

Hippocampal-dependent memory was assessed using NOR, Y-maze, and radial arm water maze (RAWM) behavioral paradigms (Figure 3F). During NOR testing, young control mice were biased toward a novel object relative to a familiar object, while young mice overexpressing cerebrovascular TNAP showed no preference (Figure 3G). No differences were observed during Y-maze testing between treatment groups (Figure 3H). In the training phase of the RAWM paradigm, all mice showed similar spatial learning ability (Figure 3I). However, young mice overexpressing cerebrovascular TNAP demonstrated impaired learning and memory for the platform location, committing more errors during the testing phase of the task compared with young control mice (Figure 3I). No difference in health metrics was observed between groups (Figures S4F–S4L). These data indicate that increased cerebrovascular TNAP impairs BBB function in the hippocampus and is a negative regulator of object and spatial memory.

Restoring the age-related increase in cerebrovascular TNAP mitigates cognitive benefits of liver-derived GPLD1 in aging

We next examined whether cognitive benefits of increased liver-derived GPLD1 in aged mice could be mitigated by restoring the age-related increase in cerebrovascular TNAP expression. Aged mice were given retro-orbital injections of liver-specific AAV encoding GPLD1 and BEC-specific AAV encoding either TNAP or Ruby control (Figure 4A). Aged mice given retro-orbital injections with liver-specific AAV encoding catalytically inactive H133N GPLD1 and BEC-specific AAV encoding Ruby were included as a negative control (Figure 4A). The observed GPLD1-mediated decrease in vascular TNAP AP activity was abrogated following viral-mediated overexpression of cerebrovascular TNAP in aged mice (Figure 4B). Hippocampal-dependent learning and memory were assessed using NOR, Y-maze, and RAWM (Figures 4A–4E). Aged mice with increased liver-derived GPLD1 and expressing vascular Ruby control exhibited a bias for the novel object and the novel arm and committed fewer errors locating a hidden platform compared with H133N GPLD1-treated aged mice expressing vascular Ruby (Figures 4C–4E). However, GPLD1-mediated cognitive benefits observed in NOR and RAWM testing, but not those observed during Y-maze testing, were abrogated in aged mice overexpressing cerebrovascular TNAP (Figures 4C–4E). Similarly, TNAP expression abrogated some of the improvements in health metrics observed in GPLD1-treated mice (Figures S4M–S4S). These *in vivo* viral-mediated overexpression and behavioral data indicate that targeting GPI-anchored cerebrovascular TNAP regulates, in part, the cognitive benefits of increased liver-derived GPLD1 on object and spatial memory in aged mice.

Targeting cerebrovascular TNAP reverses aging-related cognitive impairments

To determine the effect of selectively targeting the age-related increase in cerebrovascular TNAP expression on cognitive function, we generated aged temporally controlled BEC-specific conditional *Alpl* genetic knockout mice using a viral-mediated *in vivo* CRISPR-Cas9 approach. Aged inducible Cas9 transgenic mice were given retro-orbital injections with BEC-specific AAV encoding *Cre* and guide RNA sequences targeting *Alpl* or a safe harbor locus as a control (Figures 4F, S5A, and S5B). Decreased AP activity was confirmed on hippocampal vasculature and additional brain regions following AAV injection (Figures 4G, S5C, and S5D). Hippocampal-dependent learning and memory were assessed using NOR, Y-maze, and RAWM (Figure 4F). Abrogation of cerebrovascular TNAP expression resulted in a bias for the novel object during NOR testing and fewer errors committed locating a hidden platform during RAWM testing compared with aged control mice (Figures 4H and 4J). While no differences were observed during Y-maze testing between groups, selective improvements in overall well-being metrics were observed in the conditional knockout mice (Figures 4I and S5E–S5I).

Next, we compared the cognitive benefits of increased liver-derived GPLD1 in aged mice with the effect of inhibiting the

Please cite this article in press as: Bieri et al., Liver exerkine reverses aging- and Alzheimer's-related memory loss via vasculature, Cell (2026), https://doi.org/10.1016/j.cell.2026.01.024

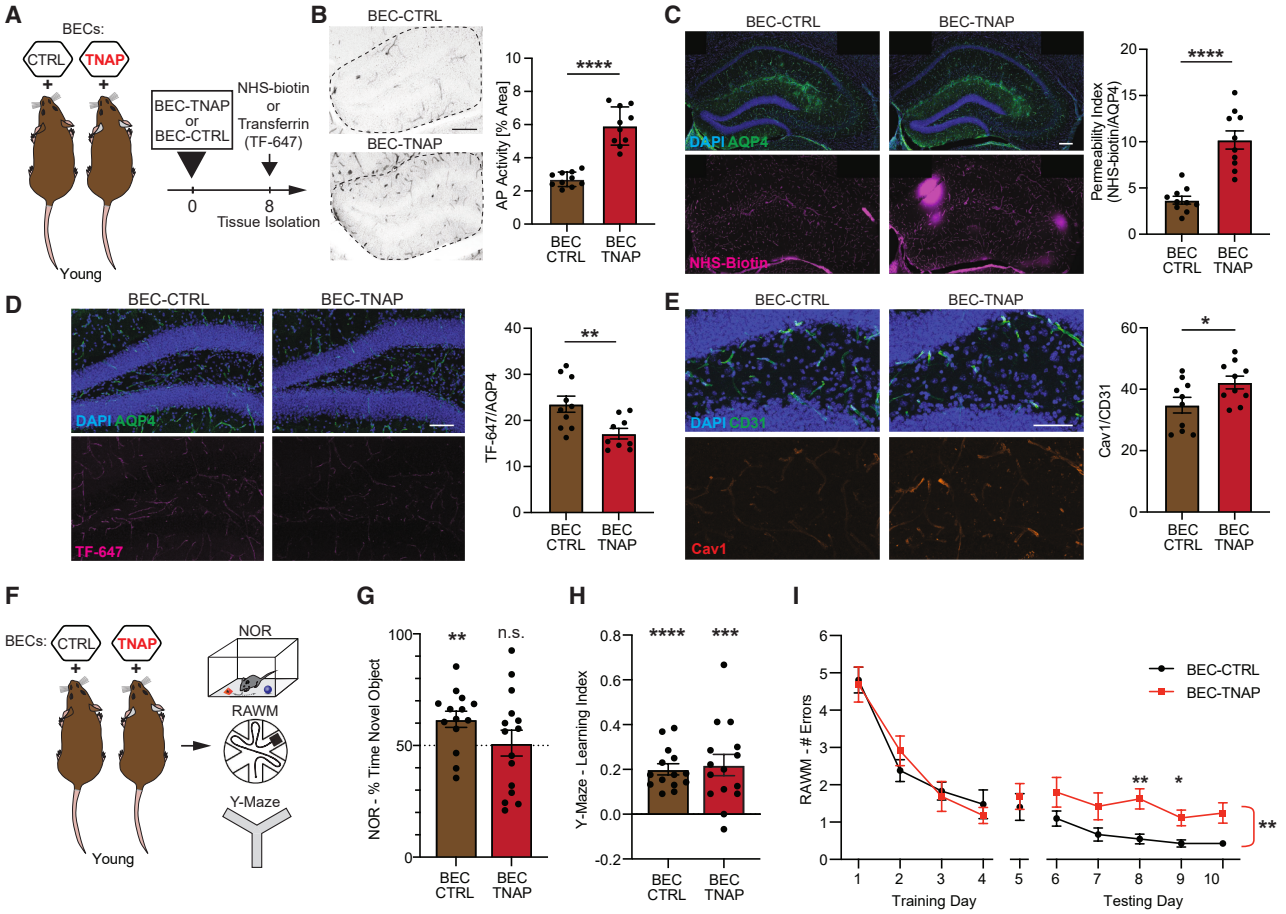

Figure 3. Mimicking the age-related increase in cerebrovascular TNAP disrupts BBB function and impairs cognition

(A) Assessment of brain vascular function and integrity in young (4–5 months) mice following selective AAV-mediated expression of TNAP on BECs.

(B) Representative images and quantification of endogenous alkaline phosphatase (AP) activity labeling in the DG region (dashed line; stitched overview image) of the hippocampus (n = 10 mice/group).

(C) Representative images and quantification of NHS-biotin leakage from hippocampal blood vessels.

(D) Representative images and quantification of labeled transferrin (TF-647) uptake by hippocampal blood vessels.

(E) Representative images and quantification of Caveolin-1 (Cav1) immunostaining of hippocampal blood vessels (n = 9–10 mice/group).

(F) Behavioral assessment in young (4–5 months) mice following BEC-specific overexpression of TNAP.

(G) Object recognition memory was measured using novel object recognition (NOR) as percent time exploring the novel object (n = 14–15 mice/group).

(H) Spatial working memory was measured in the Y-maze task as the discrimination index for the novel arm. (n = 14–15 mice/group.)

(I) Hippocampal-dependent spatial learning and memory were evaluated by radial arm water maze (RAWM) as the number of errors committed while attempting to find a hidden escape platform (n = 14–15 mice/group).

Data shown as mean ± SEM. Scale bar, 100 μm. Statistical analysis was performed using t test (B–E), a one-sample t test versus 50% (G) or 0 (H), and a two-way ANOVA with Šidák's post hoc test (I); $^{*}p < 0.05$, $^{**}p < 0.01$, $^{***}p < 0.001$, $^{****}p < 0.0001$.

See also Figure S4.

age-related increase in vascular TNAP activity using a more therapeutically tractable pharmacological approach. Aged mice given HDTVI with expression constructs encoding catalytically inactive H133N GPLD1 were administered an orally bioavailable non-brain penetrant TNAP inhibitor (TNAPi) (SBI-425)[32] or vehicle control in the chow (Figure 4K). Aged mice injected with expression constructs encoding GPLD1 and given control food were included as a positive control for GPLD1-mediated cognitive benefits (Figure 4J). Decreased AP activity was confirmed on hippocampal vasculature following TNAPi treatment (Figure 4L). Inhibition of TNAP activity resulted in cognitive improvements in object memory during NOR testing and spatial memory during RAWM testing compared with aged control mice, similar in magnitude to aged animals with increased liver-derived GPLD1 (Figures 4M and 4O). While aged GPLD1-treated mice exhibited improvements in working memory during Y-maze testing, no change was observed following TNAPi treatment (Figure 4N). Selective improvements in overall well-being metrics were detected in aged mice following inhibition of TNAP activity or with increased liver-derived GPLD1 (Figures S5J–S5P). Collectively, these behavioral data indicate that targeting vascular TNAP can in part rescue object and

Please cite this article in press as: Bieri et al., Liver exerkine reverses aging- and Alzheimer's-related memory loss via vasculature, Cell (2026), https://doi.org/10.1016/j.cell.2026.01.024

CellPress
OPEN ACCESS

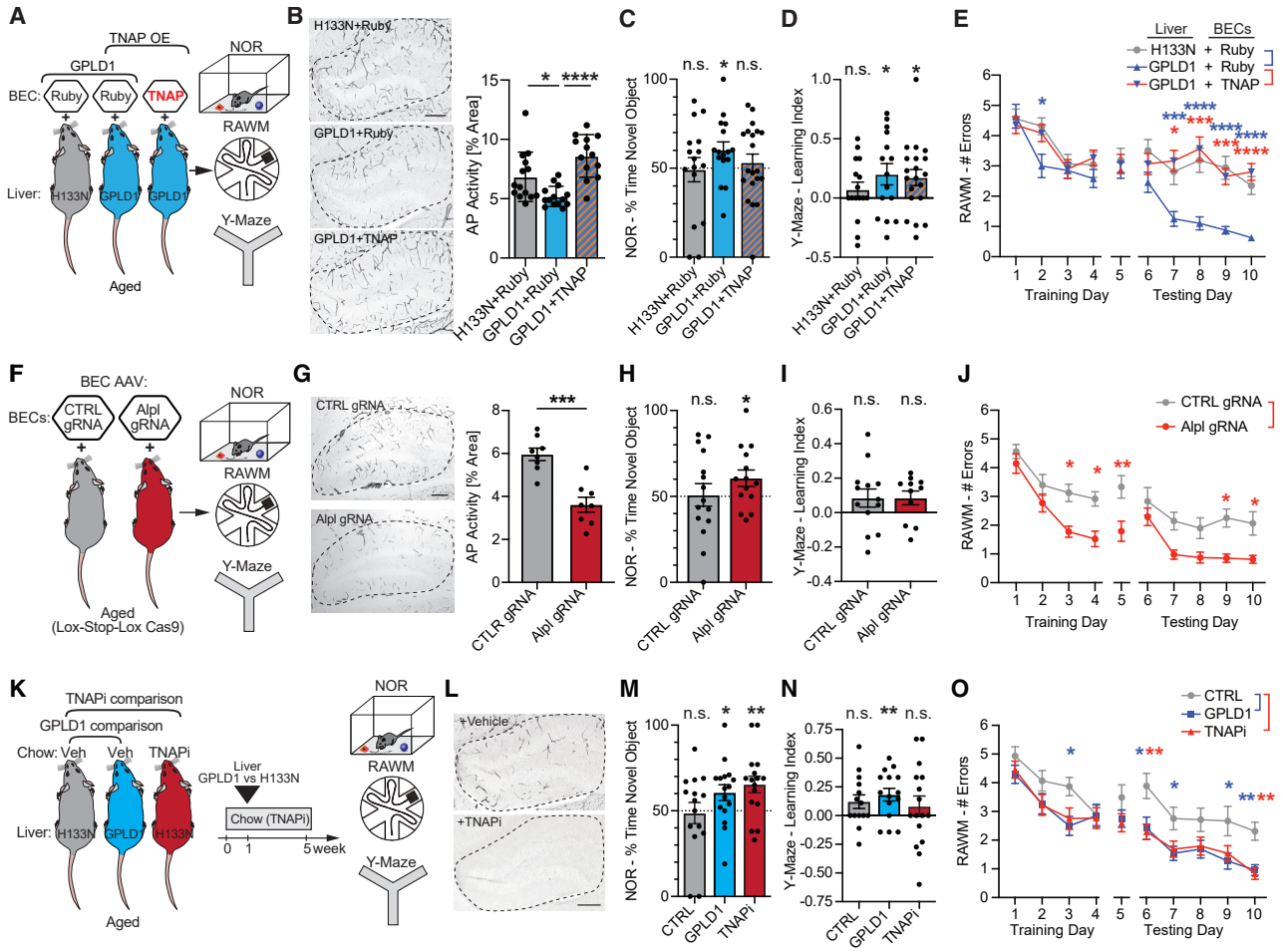

Figure 4. Increasing cerebrovascular TNAP mitigates the cognitive benefits of liver-derived GPLD1, whereas targeting TNAP reverses aging-related cognitive impairments

(A) AAV-mediated liver overexpression of GPLD1 or inactive H133N GPLD1 in aged (22–24 months) mice in combination with BEC-targeted overexpression of TNAP or Ruby2.

(B) Representative images and quantification of endogenous alkaline phosphatase (AP) activity labeling in the DG region (dashed line; stitched overview image) of the hippocampus (n = 13–15 mice/group).

(C) Object recognition memory was measured using NOR as percent time exploring the novel object (n = 16–20 mice/group).

(D) Spatial working memory was measured in the Y-maze task as the discrimination index for the novel arm. (n = 16–20 mice/group).

(E) Hippocampal-dependent spatial learning and memory were evaluated by RAWM as the number of errors committed while attempting to find a hidden escape platform (n = 16–20 mice/group).

(F) BEC-TNAP abrogation in aged transgenic mice (20–22 months) following AVV-mediated delivery of Alpl or safe harbor control gRNAs.

(G) Representative images and quantification of endogenous AP labeling in the DG (n = 8 mice/group).

(H) Object recognition memory was assessed using NOR (n = 14–15 mice/group)

(I) Spatial working memory was assessed using Y-maze (n = 11–13 mice/group).

(J) Spatial learning and memory were evaluated by RAWM (n = 14–15 mice/group).

(K) Aged mice (22–24 months) with liver overexpression of GPLD1, inactive H133N GPLD1 (control), or systemic TNAP inhibition via SBI-425 administered in specialized chow.

(L) Representative images of endogenous AP activity labeling in aged mouse brain sections treated with the TNAP inhibitor.

(M) Object recognition memory was assessed using NOR (n = 15–17 mice/group)

(N) Spatial working memory was assessed using Y-maze (n = 15–17 mice/group).

(O) Spatial learning and memory were evaluated by RAWM (n = 15–17 mice/group).

Data shown as mean ± SEM. Scale bar, 200 μm. Statistical analysis was performed using one-way ANOVA with Šidák's post hoc test (B), t test (G), one-sample t test versus 50% (C, H, and M) or 0 (D, I, and N), and two-way ANOVA with Šidák's post hoc test (E, J, and O); $^{*}p < 0.05$, $^{**}p < 0.01$, $^{***}p < 0.001$, $^{****}p < 0.0001$. See also Figures S4 and S5.

Please cite this article in press as: Bieri et al., Liver exerkine reverses aging- and Alzheimer's-related memory loss via vasculature, Cell (2026), https://doi.org/10.1016/j.cell.2026.01.024

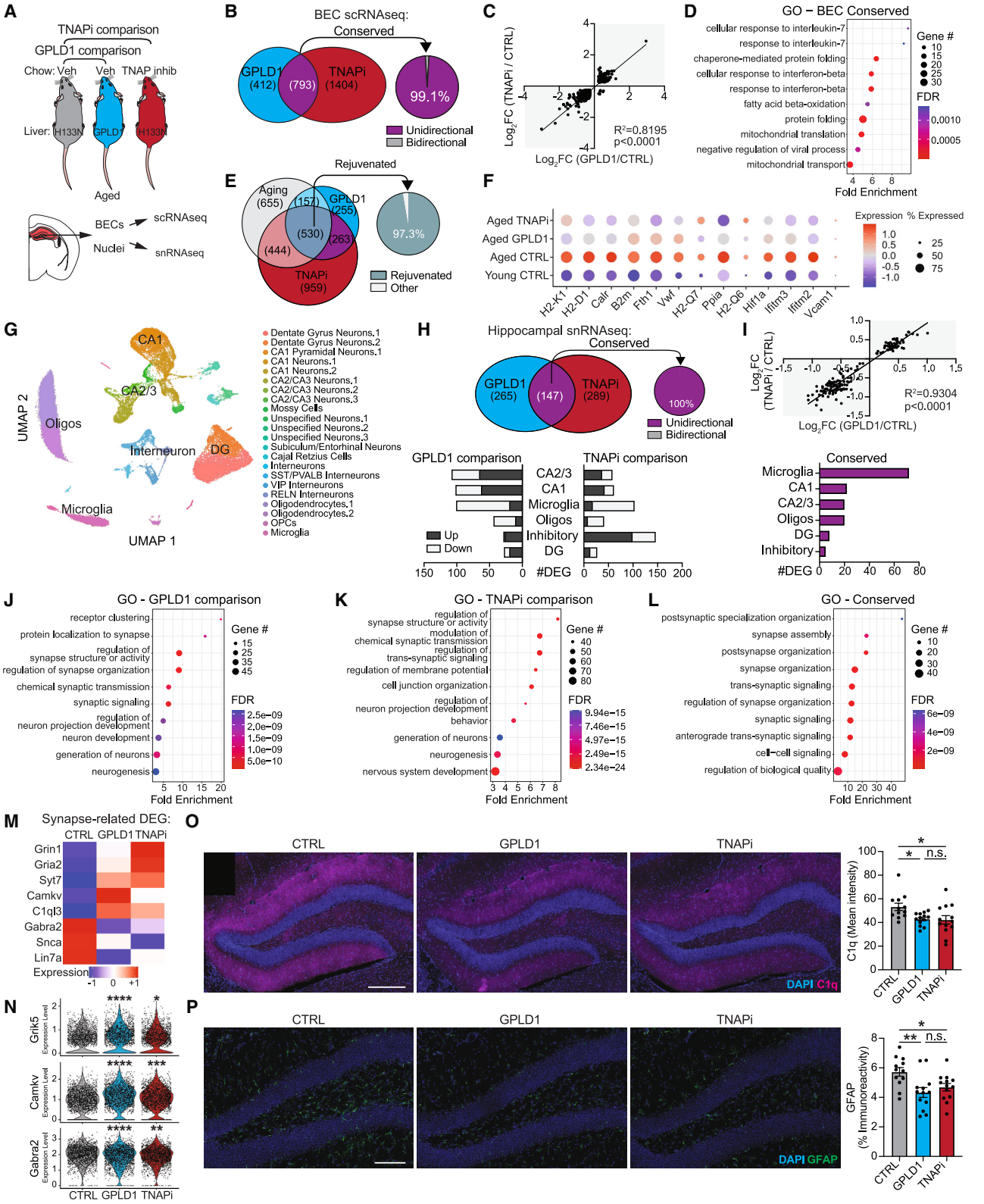

(legend on next page)

Please cite this article in press as: Bieri et al., Liver exerkine reverses aging- and Alzheimer's-related memory loss via vasculature, Cell (2026), https://doi.org/10.1016/j.cell.2026.01.024

spatial memory at old age, comparable with the cognitive benefits of increased liver-derived GPLD1.

Inhibiting TNAP activity recapitulates hippocampal transcriptional signatures of liver-derived GPLD1 in aging

To gain mechanistic insight, we further compared the cellular and molecular changes induced in both hippocampal BECs and parenchyma of aged mice following vascular TNAP inhibition and increased liver-derived GPLD1 expression using scRNA-seq and single-nucleus RNA sequencing (snRNA-seq) (Figure 5A).

First, we isolated BECs from hippocampi of aged mice following TNAPi treatment and detected prominent transcriptional changes compared with BECs from aged controls (Figures 5B and S3A–S3E). Subsequently, we focused our analysis on conserved DEGs following both GPLD1 and TNAPi treatments and observed a significant overlap, with 65% of DEGs in the GPLD1 treatment group conserved with the TNAPi group (Figures 5B and 5C). GO analysis of conserved DEGs identified inflammatory processes, energy metabolism, and proteostasis as shared biological processes between the two interventions (Figures 5D, S3H, and S3I). Moreover, we observed an overlap of 530 DEGs between the aging, GPLD1, and TNAPi comparisons, of which 97.3% were restored to a more youthful level (Figure 5E). Several of the DEGs identified in our scRNA-seq dataset, including *Vcam1* and *Ppia* (cyclophilin A), have previously been implicated in brain aging and vascular dysfunction (Figure 5F).[19,33,34] Collectively, these single-cell transcriptomics data indicate that increasing liver-derived GPLD1 as well as TNAP inhibition, in part, restores more youthful transcriptional signatures in BECs from the aged hippocampus. Since interventions that restore brain vascular dysfunction have been shown to regulate neuroinflammatory, regenerative, and cognitive function in the aged brain,[19,29,30,35] we next surveyed gene expression changes of cell types residing in the brain parenchyma using a complementary snRNA-seq approach.

Nuclei were isolated from hippocampi of aged mice expressing liver-derived GPLD1, aged mice treated with TNAPi, or control mice expressing H133N GPLD1 and analyzed by snRNA-seq (Figures 5A and 5G). A total of 22 cell clusters were identified, and populations were compared across treatment groups (Figures 5H and S6A–S6D). We detected prominent transcriptional changes in neuronal populations and microglia in the hippocampus of aged mice following either TNAPi treatment or increased liver-derived GPLD1 expression compared with aged control-treated mice expressing liver-derived H133N GPLD1 (Figures 5H and 5I). Of the transcriptional changes induced following TNAP inhibition, about 30% were conserved with changes induced by increased liver-derived GPLD1 (Figures 5H, 5I, S6E, and S6F). We found that transcriptional responses in the hippocampus are encoded in different cell types with a combination of upregulated and downregulated genes, with DEGs largely unique to cell type (Figures 5H and S6G–S6I). GO analysis of DEGs between TNAPi and control treatment groups identified synaptic plasticity-related biological processes, consistent with changes observed following increased liver-derived GPLD1 expression (Figures 5J, 5K, S6J, and S6K).

Focused analysis on conserved DEGs that change following both TNAPi treatment and increased liver-derived GPLD1 compared with aged control-treated mice expressing liver-derived H133N GPLD1 (Figures 5H and 5I) revealed that most of the conserved transcriptional responses were unique to cell type, with microglia and excitatory neuronal populations (Cornu Ammonis, CA1/2/3) exhibiting the largest changes (Figures 5I, S6E, and S6I). GO analysis of DEGs identified

Figure 5. Inhibiting TNAP activity recapitulates hippocampal transcriptional signatures of GPLD1 treatment in aging

(A) Aged mice (22–24 months) with liver overexpression of GPLD1, inactive H133N GPLD1 (control), or systemic TNAP inhibition via SBI-425 administration in specialized chow. Hippocampal BECs were profiled using scRNA-seq. Parenchymal gene expression was assessed using snRNA-seq of the hippocampus.

(B) Venn diagram (left) of DEGs in BECs for the GPLD1 (blue) and TNAPi comparisons (red). Pie chart (right) of 793 overlapping DEGs between GPLD1 and TNAPi comparisons separated by unidirectional versus bidirectional changes.

(C) Scatterplot of conserved DEGs in BECs for the GPLD1 (*x* axis) and TNAPi comparisons (*y* axis).

(D) GO terms of biological processes associated with conserved DEGs in BECs.

(E) Venn diagram (left) of the number of DEGs in BECs, including a young versus aged comparison. Pie chart (right) of the 530 rejuvenated DEGs, which are restored toward a more youthful state in the GPLD1 and TNAPi comparisons.

(F) Dot plot of rejuvenated DEGs in BECs from GPLD1 and TNAPi treatment groups.

(G) UMAP of identified cell types in the hippocampal snRNA-seq analysis.

(H) Venn diagrams (top left) and bar graphs (bottom) of parenchymal DEGs by cell type for GPLD1 (blue) and TNAPi comparison (red). Pie chart (top right) of 147 overlapping DEGs between GPLD1 and TNAPi comparisons (top) separated by unidirectional (purple) versus bidirectional changes. Overlapping unidirectionally changing DEGs between the GPLD1 and TNAPi comparisons are referred to as the conserved signature.

(I) Scatterplot (top) of conserved parenchymal DEGs for the GPLD1 (*x* axis) and TNAPi comparisons (*y* axis). Bar graph (bottom) of conserved parenchymal DEGs by cell type.

(J) Top GO terms of biological processes associated with parenchymal DEGs for the GPLD1 comparison.

(K) Top GO terms of biological processes associated with parenchymal DEGs for the TNAPi comparison.

(L) Top GO terms of biological processes associated with conserved parenchymal DEGs.

(M) Heatmap of DEGs selected from synapse-related GO terms.

(N) Violin plots of conserved DEGs (Grik5, Camkv, and Gabra2) between the GPLD1 or TNAPi comparisons.

(O) Representative images and quantification of C1q immunolabeling in the DG region of the hippocampus (n = 12–13 mice/group). Scale bar, 200 μm.

(P) Representative images and quantification of GFAP immunolabeling in the DG (n = 12–13 mice/group). Scale bar, 100 μm.

Data shown as mean ± SEM. Statistical analysis was performed using linear regression (C and I), ANOVA with Šidák's post hoc test (O and P), and Model-based Analysis of Single-cell Transcriptomics (MAST) analysis for control versus GPLD1 treatment and control versus TNAPi treatment comparisons (N); $^{*}p < 0.05$, $^{**}p < 0.01$, $^{****}p < 0.0001$.

See also Figures S3 and S6.

Please cite this article in press as: Bieri et al., Liver exerkine reverses aging- and Alzheimer's-related memory loss via vasculature, Cell (2026), https://doi.org/10.1016/j.cell.2026.01.024

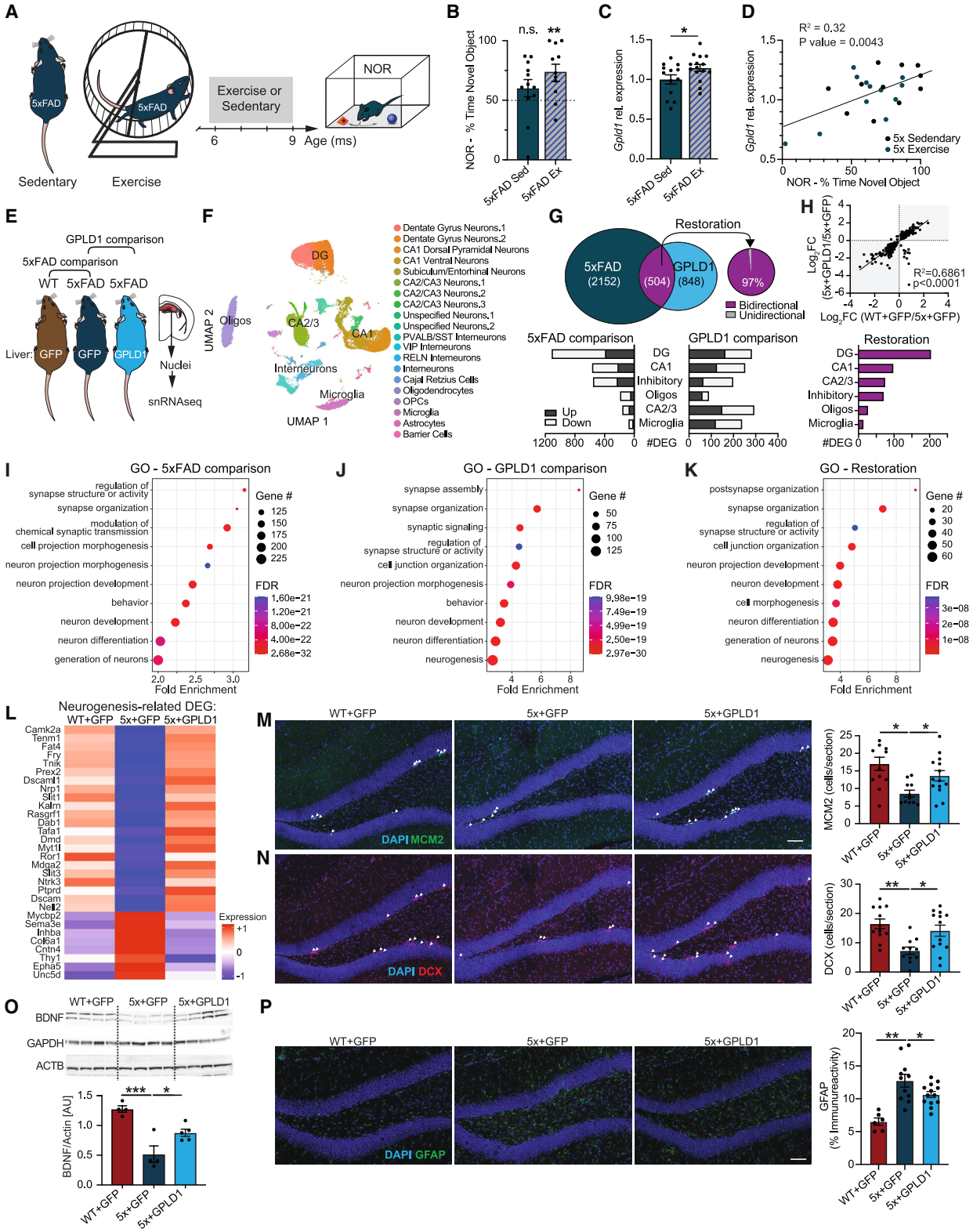

Figure 6. Liver-derived GPLD1 increases with exercise and rescues hippocampal transcriptional signatures in models of AD pathology

(A) Adult 5xFAD mice underwent a 12-week-long voluntary exercise intervention, followed by behavioral testing (9–10 months).

(B) Object recognition memory was measured using NOR as the percent of time exploring the novel object.

(legend continued on next page)

Please cite this article in press as: Bieri et al., Liver exerkine reverses aging- and Alzheimer's-related memory loss via vasculature, Cell (2026), https://doi.org/10.1016/j.cell.2026.01.024

synaptic plasticity- and behavior-related biological processes, further supporting the cognitive improvements we observed in the GPLD1 and TNAPi treatment groups (Figures 4K–4O and 5J–5N). Since we observed significant gene expression changes in the microglia cluster, we next complemented transcriptomics data by assessing levels of Complement component 1q (C1q), a microglia-derived complement factor involved in synaptic pruning and known to increase with age.[36] We observed reduced C1q expression in the aged hippocampus following both TNAPi treatment and increased liver-derived GPLD1 compared with the control group (Figure 5O). Due to technical limitations, astrocytes were not robustly captured in our snRNA-seq approach; therefore, we assessed levels of astrogliosis in the aged hippocampus and detected decreased Glial fibrillary acidic protein (GFAP) expression in both GPLD1 and TNAPi treatment groups (Figure 5P). Together, these data indicate that targeting TNAP activity can partially recapitulate the transcriptomic signature observed in the hippocampus of aged mice with increased liver-derived GPLD1.

Liver-derived GPLD1 increases with exercise and rescues hippocampal transcriptional signatures in a model of AD pathology

Aging drives vulnerability to dementia-related neurodegenerative disorders, such as AD.[37] Correspondingly, we next explored the translational potential of increased liver-derived GPLD1 in ameliorating AD pathology and associated cognitive deficits using a transgenic AD mouse model. We selected the 5xFAD model expressing the human Amyloid-β precursor protein (APP) and Presenilin-1 (PSEN1) transgenes with five AD-linked mutations within APP/PSEN1,[8,38] which represents a transgenic model with relatively early onset of AD pathology and cognitive deficits observed prior to normal aging-related cognitive decline.[8,38,39] We sought to utilize the fast-progressing nature of AD pathology in the 5xFAD model to delineate between the beneficial effects of Gpld1 that target aging-specific impairments in aged wild-type (WT) mice from those that target AD pathology in 5xFAD mice at young ages normally devoid of natural age-related cognitive impairments. We exercised mature 5xFAD mice for 3 months using voluntary wheel running (Figure 6A). Hippocampal-dependent cognitive function was assessed using NOR. Exercised 5xFAD mice spent significantly more time with the novel object compared with their sedentary counterparts (Figure 6B). We detected increased GPLD1 expression in the liver (the main source of circulating GPLD1)[16,40] of exercised versus sedentary 5xFAD mice (Figure 6C), of which GPLD1 expression was positively correlated with performance in the NOR task (Figure 6D). These data indicate exercise increases liver GPLD1 expression concurrent with cognitive improvements in mature 5xFAD mice.

To investigate the cellular and molecular changes elicited in the hippocampus of 5xFAD mice by increased liver-derived GPLD1, we performed snRNA-seq analysis. Mature 5xFAD mice were given HDTVI with expression constructs encoding GPLD1 or GFP control (Figure 6E). Age-matched WT littermate control mice given HDTVI with expression constructs encoding GFP were included to assess baseline changes induced by AD pathology (Figure 6E). A total of 20 cell clusters were identified, and populations were compared across genotype and treatment groups (Figures 6F and S7A–S7D). We detected pronounced transcriptional changes in excitatory neuronal populations (dentate gyrus [DG] and CA1) in the hippocampus of 5xFAD compared with WT control mice (Figure 6G), as well as following increased liver-derived GPLD1 expression (Figure 6G). Of the transcriptional changes detected in 5xFAD, close to 30% were restored toward WT conditions in the GPLD1-treated 5xFAD group (Figures 6G, 6H, S7E, and S7F). We found that transcriptional responses detected in the hippocampus are encoded in different cell types with a combination of upregulated and downregulated genes that are largely unique to cell type (Figures 6G, S7G, and S7H). GO analysis of DEGs in 5xFAD mice and following GPLD1 treatment identified neurogenesis- and synaptic-related biological processes (Figures 6I, 6J, S7I, and S7J).

(C) Liver GPLD1 expression was measured by RT-qPCR analysis.
(D) Correlation of liver GPLD1 expression with cognitive performance in the NOR task in exercised and sedentary 5xFAD mice.
(E) snRNA-seq gene expression profiling of hippocampal parenchymal cells from 5xFAD mice or WT littermates with liver overexpression of GPLD1 or GFP control.
(F) UMAP of identified cell types in the hippocampal snRNA-seq analysis.
(G) Venn diagrams, pie chart (top), and bar graph (bottom) representations of DEGs across different cell types for the 5xFAD (WT versus 5xFAD control, navy blue) and GPLD1 comparison (5xFAD+GPLD1 versus 5xFAD+GFP; light blue). Bidirectionally changing DEGs (purple) reversed to the WT condition are referred to as the restoration signature.
(H) Scatterplot (top) of 504 overlapping DEGs between the 5xFAD (*x* axis) and GPLD1 comparisons (*y* axis). Bar graph (bottom) of the restoration DEGs by cell type.
(I) Top GO terms of biological processes for the 5xFAD comparison.
(J) Top GO terms of biological processes for the GPLD1 comparison.
(K) Top GO terms of biological processes associated with restored DEGs.
(L) Heatmap of DEGs selected from neurogenesis-related GO terms.
(M) Representative images and quantification of immunolabeling of the neural progenitor cell marker MCM2 (green) in the DG region of the hippocampus (n = 11–13 mice/group).
(N) Representative images and quantification of doublecortin (DCX, red) immunolabeling in the DG (n = 11–13 mice/group).
(O) Representative immunoblots and quantification of BDNF in hippocampal lysates (n = 4–5 mice/group).
(P) Representative images and quantification of GFAP immunolabeling in the DG (n = 6–13 mice/group).
Data shown as mean ± SEM. Scale bar, 100 μm. Statistical analysis was performed using a one-sample *t* test versus 50% (B), *t* test (C), linear regression (D and H), and ANOVA with Šidák's post hoc test (M–P) and MAST analysis; $^{*}p < 0.05$, $^{**}p < 0.01$.
See also Figure S7.

Please cite this article in press as: Bieri et al., Liver exerkine reverses aging- and Alzheimer's-related memory loss via vasculature, Cell (2026), https://doi.org/10.1016/j.cell.2026.01.024

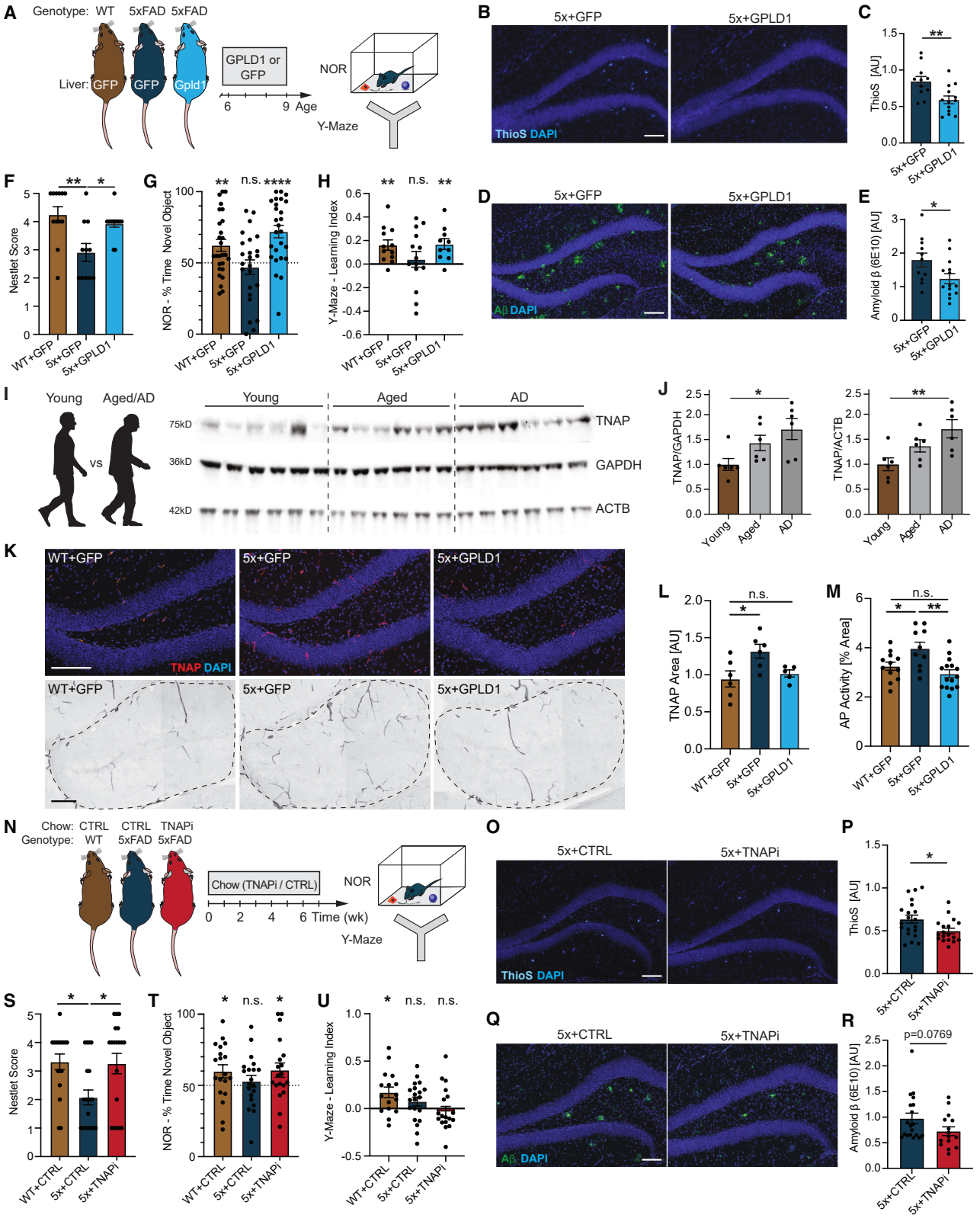

(legend on next page)

Please cite this article in press as: Bieri et al., Liver exerkine reverses aging- and Alzheimer's-related memory loss via vasculature, Cell (2026), https://doi.org/10.1016/j.cell.2026.01.024

Subsequently, we focused our analysis on DEGs that change in 5xFAD mice but are rescued following GPLD1 treatment compared with WT control conditions (Figures 6H, S7E, and S7F). Most of the rescued transcriptional responses were unique to cell type, with excitatory neuronal populations (DG and CA1) exhibiting the largest changes (Figures 6H, S7E, and S7K). GO analysis of DEGs identified neurogenesis- and synaptic-related biological processes (Figures 6K and 6L). Consistent with transcriptomics data, we observed increased adult neurogenesis (MCM2-positive neural progenitors and doublecortin [DCX]-positive newly born neurons) and elevated levels of Brain-derived neurotrophic factor (BDNF), a neurotrophic factor involved in synaptic plasticity, in the hippocampus of GPLD1-treated 5xFAD mice (Figures 6M–6O). Additionally, we surveyed the microglia cluster and observed a decrease in the expression of several disease-associated microglia (DAMs) markers and inflammatory genes previously reported in mouse models of AD pathology[41] in GPLD1-treated compared with control 5xFAD mice (Figure S7L). Lastly, we assessed levels of astrogliosis in the hippocampus and detected decreased GFAP expression (Figure 6P). These transcriptomics data indicate that increasing liver-derived GPLD1 rescues hippocampal transcriptional signatures induced in a mouse model of AD pathology.

Increasing liver-derived GPLD1 or inhibiting TNAP activity in mice ameliorates AD pathology and cognitive deficits

AD pathology in 5xFAD mice has been shown to be amenable to exercise, reducing β-amyloid (Aβ) burden and improving cognitive function following wheel running.[8] Therefore, we assessed hippocampal changes in Aβ pathology and cognitive deficits in 5xFAD mice overexpressing liver-derived GPLD1, 5xFAD mice expressing GFP, or WT littermate controls expressing GFP (Figure 7A). We observed decreased Thioflavin S-positive amyloid deposits and Aβ expression in GPLD1-treated 5xFAD mice compared with GFP control 5xFAD mice (Figures 7B–7E). We examined APP processing in the hippocampus and cortex and observed a decrease in the C-terminal fragment with no changes in full-length APP levels (Figures S8A–S8J), indicating changes in APP processing in GPLD1-treated 5xFAD mice. Additionally, we assessed well-being metrics, including nest-building scoring and hippocampal-dependent memory by NOR and Y-maze and observed functional improvements in nest formation, object memory, and working memory in 5xFAD mice following GPLD1 treatment (Figures 7F–7H). In an independent cohort of mice, we assessed spatial learning and memory using the active place avoidance task and observed impairments in 5xFAD compared with WT littermate controls that were, in part, restored in 5xFAD mice following increased liver-derived GPLD1 (Figures S8K–S8N). Functional benefits of increased liver-derived GPLD1 in 5xFAD mice were comparable with baseline levels observed in age-matched WT GFP control animals (Figures 7F–7H and S8O–S8R).

To determine whether GPI-anchored GPLD1 targets mediating cognitive rejuvenation could similarly ameliorate AD pathology, we first assessed TNAP expression in the brains of older adults and AD individuals and observed elevated levels compared with healthy young humans by western blot analysis (Figures 7I and 7J). Next, we examined changes in TNAP expression and AP activity in the hippocampus of GPLD1-treated 5xFAD mice and observed a reduction following increased liver-derived GPLD1 compared with 5xFAD mice expressing GFP (Figures 7K–7M). Consequently, we investigated the effect of targeting TNAP activity in 5xFAD mice on Aβ pathology and cognitive function. Mature 5xFAD mice were administered TNAPi or vehicle control in the food (Figure 7N). Age-matched WT littermate control mice given control food were included to assess baseline changes due to AD pathology (Figure 7N). We assessed well-being metrics by nest-building scoring and hippocampal-dependent memory by NOR and Y-maze. Inhibition of TNAP activity in 5xFAD mice resulted in decreased Thioflavin S-positive amyloid deposits and Aβ expression (Figures 7O–7R), and functional improvements in nest formation and object memory, but not working memory, compared with control

Figure 7. Increasing liver-derived GPLD1 or inhibiting TNAP activity in mice ameliorates AD pathology and cognitive deficits

(A) Cognitive behavioral testing of 5xFAD mice or WT littermates with liver overexpression of GPLD1 or GFP control (9–10 months).

(B and C) Representative images (B) and quantification (C) of thioflavin S (ThioS) amyloid plaque staining in the DG region of the hippocampus of 5xFAD mice overexpressing liver GPLD1 or GFP control (n = 11–13 mice/group).

(D and E) Representative images (D) and quantification (E) of 6E10-immunolabeled amyloid plaques in the DG region of the hippocampus (n = 11–14 mice/group).

(F) Hippocampal-dependent nest-forming performance was scored from 1 (worst) to 5 (best) (n = 11–15 mice/group)

(G) Object recognition memory was measured using NOR as percent time spent exploring the novel object (n = 24–27 mice/group).

(H) Spatial working memory was measured in the Y-maze task as the discrimination index for the novel arm (n = 10–14 mice/group).

(I and J) Western blot analysis (I) and quantification (J) of TNAP in human cortical lysates from young, aged, and donors with AD (n = 6 samples/group). (J) Quantifications of TNAP normalized to GAPDH (left) or beta-actin (ACTB, right).

(K–M) Representative images (K) and quantifications of TNAP immunostaining (L) and alkaline phosphatase (AP) activity labeling (M) in the DG (dashed line; stitched overview image) (n = 5–15 mice/group).

(N) Cognitive behavioral testing and histological analysis of adult 5xFAD or WT littermate controls (11–12 months) following systemic TNAP inhibition via SBI-425 administration in specialized chow.

(O and P) Representative images (O) and quantification (P) of ThioS staining in the DG (n = 18–20).

(Q and R) Representative images (Q) and quantification (R) of 6E10 immunolabeled amyloid plaques in the DG (n = 15–19 mice/group).

(S) Nest-forming performance was assessed in TNAPi-treated 5xFAD mice (n = 17–20 mice/group).

(T) Object recognition memory was assessed using the NOR task (n = 19–20 mice/group).

(U) Spatial working memory was assessed using Y-maze (n = 16–20 mice/group).

Data shown as mean ± SEM. Scale bar, 200 μm. Statistical analysis was performed using t test (C, E, P, and R), ANOVA with Šidák's post hoc test (F, J, L, M, and S), and one-sample t test versus 50% (G and T) or 0 (H and U); $^{*}p < 0.05$, $^{**}p < 0.01$, $^{****}p < 0.0001$.

See also Figure S8.

Please cite this article in press as: Bieri et al., Liver exerkine reverses aging- and Alzheimer's-related memory loss via vasculature, Cell (2026), https://doi.org/10.1016/j.cell.2026.01.024

conditions (Figures 7S–7U and S8S–S8V). Collectively, these data indicate that increasing liver-derived GPLD1 or inhibiting activity of its GPI-anchored substrate TNAP can ameliorate Aβ pathology and cognitive deficits in an AD mouse model.

DISCUSSION

Cumulatively, our data demonstrate that the liver-derived exercise factor GPLD1 reverses memory loss in aging and models of AD pathology by targeting GPI-anchored TNAP on the brain vasculature. From a translational perspective, these data further suggest significant therapeutic potential to ameliorate neurodegenerative disease pathology, similar to the benefits of exercise but independent of physical activity.

Broad therapeutic approaches targeting cerebrovascular health during aging may be ideally situated to mitigate the progression of AD-related cognitive dysfunction. The brain vasculature shows dramatic changes in aging, including reduction in vessel density and dysregulation of BBB function.[26,42] Disruptions of cerebrovascular integrity are also now appreciated as cardinal features of AD, as highlighted by whole genome, neuropathological, neuroimaging, and cerebrospinal fluid (CSF) studies in humans.[43–46] In individuals along the AD continuum, CSF and neuroimaging markers of cerebrovascular and BBB injury are evidenced prior to overt dementia symptoms and correlate with cognitive and functional symptoms.[44] Even autosomal dominant forms of AD that are thought to represent young-onset AD pathology show cerebrovascular injury up to a decade prior to symptom onset.[47] Together, vascular disruption is an early phenomenon in aging and AD and strongly tracks with the onset and progression of cognitive symptoms in AD patients. Excitingly, the brain vasculature is amenable to blood-based interventions. As such, treatment with young blood factors or targeting pro-geronic factors has been shown to promote vascular outgrowth and restore function without the need for direct delivery into the brain.[19,22,35,48,49] In this context, GPLD1 emerges as an attractive therapeutic candidate to improve cognition, possibly via modulation of factors that influence brain vascular function. Indeed, increased activity of the GPLD1 substrate TNAP on the aging cerebrovasculature has been shown to promote disruptions in BBB function,[26] which we now functionally link to cognitive deficits in aging and mouse models of AD pathology. As such, cleavage of vascular GPI-anchored TNAP by GPLD1 points to proper transport across blood vessels to the brain as one potential cerebrovascular target by which to restore cognition in older adults and AD individuals. In fact, TNAP inhibition has been demonstrated to restore blood-brain transport in aged animals to youthful levels.[26]

While current therapeutic approaches to treat AD are predominantly focused on targeting neuropathology within the central nervous system, our work investigating a liver-to-brain exercise axis bolsters the possibility of targeting complementary molecular factors in blood and peripheral tissues to treat dementia-related neurodegenerative diseases. Our studies have significant translational potential, identifying GPI-anchored proteins downstream of GPLD1 as potential therapeutic targets. However, it should be noted that while inhibition of vascular GPI-anchored TNAP in part recapitulates cognitive benefits of liver-derived GPLD1 in aging and models of AD pathology, the benefits of GPLD1 are likely the result of targeting multiple GPI-anchored proteins across different cell types. Indeed, GPLD1-mediated cognitive benefits on working memory observed in Y-maze testing were not mitigated following increased cerebrovascular TNAP expression in aged mice. Mechanistically, the benefits of downstream GPLD1 targets may work in concert with other known exercise-induced factors, such as irisin, Insulin-like growth factor 1 (IGF1), clusterin, Platelet factor 4 (PF4), and Selenoprotein P (SEPP1).[2,3,17,50–56] Therefore, it is important for future studies to elucidate whether each factor acts through convergent or divergent cellular targets and molecular pathways. Given that individuals appear to progress along different aging trajectories,[57] it may be that successful development of future therapies aimed at restoring cognition at old age necessitates identification of convergent mechanisms whose activation may provide additive benefits of multiple exercise-induced blood factors.

More broadly, GPLD1 has recently been reported to increase in the liver and plasma of mouse models known to extend lifespan, including growth hormone receptor knockout mice, Snell dwarfs, caloric restriction, and treatment with compounds such as rapamycin.[58–60] In this context, our data raise the exciting possibility that the benefits of liver-derived GPLD1 may extend beyond cognitive rejuvenation and amelioration of neurodegenerative disease pathology in the aging brain to promote overall longevity at the organismal level.

Limitations of the study

Hippocampal snRNA-seq and BEC scRNA-seq analyses begin to dissect the mechanisms by which increased liver-derived GPLD1 promotes cognitive benefits in aging and AD mouse models. We note that, due to technical limitations, our nuclei isolation and sequencing approach did not capture sufficient numbers of astrocytes for snRNA-seq analysis. In addition, transcriptional changes in certain cell populations, such as activated microglia, are often difficult to resolve with snRNA-seq,[61] and the pooling of samples limited our ability to evaluate inter-individual variability. Although we complement the transcriptomic data with immunohistochemical analysis and observe reduced astrogliosis across conditions, these data provide limited insight into the molecular changes occurring within these cell populations. Increased TNAP activity was observed in several brain regions beyond the hippocampus. Similarly, GPLD1 treatment, as well as our viral-mediated expression approaches, targeted cerebrovascular TNAP more broadly in the brain. While our analyses focused primarily on hippocampal functions, our data suggest that the effects of GPLD1 and TNAP manipulations may extend to additional brain regions that were not investigated. In the periphery, bioinformatics analysis also identified enrichment of GPI-anchored proteinss on peripheral immune cells, implicating molecular changes involved in age-related increased systemic inflammation as additional potential downstream GPLD1 targets to improve cognition. We anticipate that these data will prompt mechanistic and translational investigations delineating the contribution of identified genes within the hippocampus and GPI-anchored proteins in the periphery in mediating cognitive

benefits observed following GPLD1 treatment in both aging and disease.

RESOURCE AVAILABILITY

Lead contact

Further information and requests for resources and reagents should be directed to and will be fulfilled by the lead contact, Dr. Saul Villeda (saul.villeda@ucsf.edu).

Materials availability

Plasmids generated in this study are available from the lead contact upon request.

Data and code availability

- The snRNA-seq and scRNA-seq datasets are available at the Gene Expression Omnibus (GEO) at accession numbers GEO: GSE304483 and GEO: GSE269061.
- This paper does not report original code.
- Additional details are available from the lead contact upon request.

ACKNOWLEDGMENTS

We thank Dr. Param Singh and Dr. Andrew Brack for critically reading the manuscript and Dr. Elizabeth Crouch and Dr. Sophia M. Shi for critical input on brain vascular analyses. This work was funded by the Simons Foundation (S.A.V.), the Bakar Family Foundation (S.A.V.), the Cure Alzheimer's Fund (S.A.V.), the Hillblom Foundation (G.B.), the Glenn Foundation (T.A.), the JSPS (Y.F.), the Japanese Biochemistry Postdoctoral Fellowship (Y.F.), the Multiple Sclerosis Foundation (A.R.P.), the Frontiers in Medical Research fellowship (K.J.B.P.), the American Federation for Aging Research (T.A.), the National Science Foundation (J.S.), the Bakar Aging Research Institute (S.A.V.), a gift from Marc and Lynne Benioff, and the National Institute on Aging (AG081038 to G.B., AG086042 to J.S., AG082414 to K.B.C. and S.A.V., and AG077770 and AG067740 to S.A.V.). We acknowledge the UCSF Parnassus Flow Core (RRID: SCR_018206) and support by the DRC Grant NIH P30 DK063720 for assistance with flow cytometry. We thank the Genomics CoLabs at the UCSF Institute for Human Genetics for assistance with snRNA-seq and the UCSF CAT core for sequencing.

AUTHOR CONTRIBUTIONS

Conceptualization, S.A.V. and G.B.; formal analysis, G.B. and K.J.B.P.; funding acquisition, S.A.V.; investigation, G.B., K.J.B.P., Y.F., T.A., J.S., A.M.H., A.R.P., K.F.-V., R.C., M.P., and L.R.; methodology, G.B.; project administration, S.A.V. and G.B.; resources, A.C.Y., K.B.C., and S.-H.J.W.; supervision, S.A.V. and G.B.; visualization, S.A.V., G.B., and K.J.B.P.; writing – original draft, S.A.V. and G.B.; writing – review and editing, S.A.V. and G.B.

DECLARATION OF INTERESTS

The Regents of the University of California have applied for a provisional patent application arising from this work, "Exercise-induced circulatory factors for amelioration of cognitive, neurological, and regenerative dysfunction during aging" (PCT/US2020/016549 Inventor S.A.V.). S.A.V. consulted for The Herrick Company, Inc. and is a cofounder of Ceiba Bio, Inc.

STAR★METHODS

Detailed methods are provided in the online version of this paper and include the following:

SUPPLEMENTAL INFORMATION

Supplemental information can be found online at https://doi.org/10.1016/j.cell.2026.01.024.

Received: May 22, 2024
Revised: August 25, 2025
Accepted: January 26, 2026

REFERENCES

1. Fan, X., Wheatley, E.G., and Villeda, S.A. (2017). Mechanisms of Hippocampal Aging and the Potential for Rejuvenation. Annu. Rev. Neurosci. *40*, 251–272. https://doi.org/10.1146/annurev-neuro-072116-031357.
2. Bieri, G., Schroer, A.B., and Villeda, S.A. (2023). Blood-to-brain communication in aging and rejuvenation. Nat. Neurosci. *26*, 379–393. https://doi.org/10.1038/s41593-022-01238-8.
3. Chow, L.S., Gerszten, R.E., Taylor, J.M., Pedersen, B.K., van Praag, H., van, Trappe, S., Febbraio, M.A., Galis, Z.S., Gao, Y., Haus, J.M., et al. (2022). Exerkines in health, resilience and disease. Nat. Rev. Endocrinol. *18*, 273–289. https://doi.org/10.1038/s41574-022-00641-2.
4. van Praag, H., Shubert, T., Zhao, C., and Gage, F.H. (2005). Exercise Enhances Learning and Hippocampal Neurogenesis in Aged Mice. J. Neurosci. *25*, 8680–8685. https://doi.org/10.1523/jneurosci.1731-05.2005.
5. Kumar, A., Rani, A., Tchigranova, O., Lee, W.-H., and Foster, T.C. (2012). Influence of late-life exposure to environmental enrichment or exercise on hippocampal function and CA1 senescent physiology. Neurobiol. Aging *33*. 828.e1–828.17. https://doi.org/10.1016/j.neurobiolaging.2011.06.023.
6. Soto, I., Graham, L.C., Richter, H.J., Simeone, S.N., Radell, J.E., Grabowska, W., Funkhouser, W.K., Howell, M.C., and Howell, G.R. (2015). APOE Stabilization by Exercise Prevents Aging Neurovascular Dysfunction and Complement Induction. PLoS Biol. *13*, e1002279. https://doi.org/10.1371/journal.pbio.1002279.
7. Speisman, R.B., Kumar, A., Rani, A., Foster, T.C., and Ormerod, B.K. (2013). Daily exercise improves memory, stimulates hippocampal neurogenesis and modulates immune and neuroimmune cytokines in aging

rats. Brain Behav. Immun. *28*, 25–43. https://doi.org/10.1016/j.bbi.2012.09.013.

8. Choi, S.H., Bylykbashi, E., Chatila, Z.K., Lee, S.W., Pulli, B., Clemenson, G.D., Kim, E., Rompala, A., Oram, M.K., Asselin, C., et al. (2018). Combined adult neurogenesis and BDNF mimic exercise effects on cognition in an Alzheimer's mouse model. Science *361*, eaan8821. https://doi.org/10.1126/science.aan8821.
9. Barnes, D.E., and Yaffe, K. (2011). The projected effect of risk factor reduction on Alzheimer's disease prevalence. Lancet Neurol. *10*, 819–828. https://doi.org/10.1016/s1474-4422(11)70072-2.
10. Hörder, H., Johansson, L., Guo, X., Grimby, G., Kern, S., Östling, S., and Skoog, I. (2018). Midlife cardiovascular fitness and dementia: A 44-year longitudinal population study in women. Neurology *90*, e1298–e1305. https://doi.org/10.1212/wnl.0000000000005290.
11. Yaffe, K., Barnes, D., Nevitt, M., Lui, L.Y., and Covinsky, K. (2001). A prospective study of physical activity and cognitive decline in elderly women: women who walk. Arch. Intern. Med. *161*, 1703–1708. https://doi.org/10.1001/archinte.161.14.1703.
12. Müller, S., Preische, O., Sohrabi, H.R., Gräber, S., Jucker, M., Ringman, J.M., Martins, R.N., McDade, E., Schofield, P.R., Ghetti, B., et al. (2018). Relationship between physical activity, cognition, and Alzheimer pathology in autosomal dominant Alzheimer's disease. Alzheimers Dement. *14*, 1427–1437. https://doi.org/10.1016/j.jalz.2018.06.3059.
13. Cunningham, C., O' Sullivan, R.O., Caserotti, P., and Tully, M.A. (2020). Consequences of physical inactivity in older adults: A systematic review of reviews and meta-analyses. Scand. J. Med. Sci. Sports *30*, 816–827. https://doi.org/10.1111/sms.13616.
14. Kohl, H.W., Craig, C.L., Lambert, E.V., Inoue, S., Alkandari, J.R., Leetongin, G., and Kahlmeier, S.; Lancet Physical Activity Series Working Group (2012). The pandemic of physical inactivity: global action for public health. Lancet *380*, 294–305. https://doi.org/10.1016/s0140-6736(12)60898-8.
15. Gomes, M., Figueiredo, D., Teixeira, L., Poveda, V., Paúl, C., Santos-Silva, A., and Costa, E. (2017). Physical inactivity among older adults across Europe based on the SHARE database. Age Ageing *46*, 71–77. https://doi.org/10.1093/ageing/afw165.
16. Horowitz, A.M., Fan, X., Bieri, G., Smith, L.K., Sanchez-Diaz, C.I., Schroer, A.B., Gontier, G., Casaletto, K.B., Kramer, J.H., Williams, K.E., et al. (2020). Blood factors transfer beneficial effects of exercise on neurogenesis and cognition to the aged brain. Science *369*, 167–173. https://doi.org/10.1126/science.aaw2622.
17. De Miguel, Z.D., Khoury, N., Betley, M.J., Lehallier, B., Willoughby, D., Olsson, N., Yang, A.C., Hahn, O., Lu, N., Vest, R.T., et al. (2021). Exercise plasma boosts memory and dampens brain inflammation via clusterin. Nature *600*, 494–499. https://doi.org/10.1038/s41586-021-04183-x.
18. Norevik, C.S., Huuha, A.M., Røsbjørgen, R.N., Hildegard Bergersen, L., Jacobsen, K., Miguel-dos-Santos, R., Ryan, L., Skender, B., Moreira, J.B.N., Kobro-Flatmoen, A., et al. (2023). Exercised blood plasma promotes hippocampal neurogenesis in the Alzheimer's disease rat brain. J. Sport Heal. Sci. *13*, 245–255. https://doi.org/10.1016/j.jshs.2023.07.003.
19. Tabula; Muris Consortium; Overall coordination; Logistical coordination; Organ collection and processing; Library preparation and sequencing; Computational data analysis; Cell type annotation; Writing group; Supplemental text writing group; Principal investigators (2018). Single-cell transcriptomics of 20 mouse organs creates a Tabula Muris. Nature *562*, 367–372. https://doi.org/10.1038/s41586-018-0590-4.
20. Karlsson, M., Zhang, C., Méar, L., Zhong, W., Digre, A., Katona, B., Sjöstedt, E., Butler, L., Odeberg, J., Dusart, P., et al. (2021). A single–cell type transcriptomics map of human tissues. Sci. Adv. *7*, eabh2169. https://doi.org/10.1126/sciadv.abh2169.
21. Yousef, H., Czupalla, C.J., Lee, D., Chen, M.B., Burke, A.N., Zera, K.A., Zandstra, J., Berber, E., Lehallier, B., Mathur, V., et al. (2019). Aged blood impairs hippocampal neural precursor activity and activates microglia via brain endothelial cell VCAM1. Nat. Med. *25*, 988–1000. https://doi.org/10.1038/s41591-019-0440-4.
22. Chen, M.B., Yang, A.C., Yousef, H., Lee, D., Chen, W., Schaum, N., Lehallier, B., Quake, S.R., and Wyss-Coray, T. (2020). Brain Endothelial Cells Are Exquisite Sensors of Age-Related Circulatory Cues. Cell Rep. *30*, 4418–4432.e4. https://doi.org/10.1016/j.celrep.2020.03.012.
23. Millán, J.L., and Whyte, M.P. (2016). Alkaline Phosphatase and Hypophosphatasia. Calcif. Tissue Int. *98*, 398–416. https://doi.org/10.1007/s00223-015-0079-1.
24. Goettsch, C., Strzelecka-Kiliszek, A., Bessueille, L., Quillard, T., Mechtouff, L., Pikula, S., Canet-Soulas, E., Millan, J.L., Fonta, C., and Magne, D. (2022). TNAP as a therapeutic target for cardiovascular calcification: a discussion of its pleiotropic functions in the body. Cardiovasc. Res. *118*, 84–96. https://doi.org/10.1093/cvr/cvaa299.
25. Millán, J.L. (2006). Alkaline Phosphatases: Structure, Substrate Specificity and Functional Relatedness to Other Members of a Large Superfamily of Enzymes. Purinergic Signal. *2*, 335–341. https://doi.org/10.1007/s11302-005-5435-6.
26. Yang, A.C., Stevens, M.Y., Chen, M.B., Lee, D.P., Stähli, D., Gate, D., Contrepois, K., Chen, W., Iram, T., Zhang, L., et al. (2020). Physiological blood–brain transport is impaired with age by a shift in transcytosis. Nature *583*, 425–430. https://doi.org/10.1038/s41586-020-2453-z.
27. Raikwar, N.S., Bowen, R.F., and Deeg, M.A. (2005). Mutating His29, His125, His133 or His158 abolishes glycosylphosphatidylinositol-specific phospholipase D catalytic activity. Biochem. J. *391*, 285–289. https://doi.org/10.1042/bj20050656.
28. Scallon, B.J., Fung, W.J., Tsang, T.C., Li, S., Kado-Fong, H., Huang, K.S., and Kochan, J.P. (1991). Primary Structure and Functional Activity of a Phosphatidylinositol-Glycan-Specific Phospholipase D. Science *252*, 446–448. https://doi.org/10.1126/science.2017684.
29. Park, M.H., Lee, J.Y., Park, K.H., Jung, I.K., Kim, K.-T., Lee, Y.-S., Ryu, H.-H., Jeong, Y., Kang, M., Schwaninger, M., et al. (2018). Vascular and Neurogenic Rejuvenation in Aging Mice by Modulation of ASM. Neuron *100*, 167–182.e9. https://doi.org/10.1016/j.neuron.2018.09.010.
30. Shi, S.M., Suh, R.J., Shon, D.J., Garcia, F.J., Buff, J.K., Atkins, M., Li, L., Lu, N., Sun, B., Luo, J., et al. (2025). Glycocalyx dysregulation impairs blood–brain barrier in ageing and disease. Nature *639*, 985–994. https://doi.org/10.1038/s41586-025-08589-9.
31. Ravindra Kumar, S.R., Miles, T.F., Chen, X., Brown, D., Dobreva, T., Huang, Q., Ding, X., Luo, Y., Einarsson, P.H., Greenbaum, A., et al. (2020). Multiplexed Cre-dependent selection yields systemic AAVs for targeting distinct brain cell types. Nat. Methods *17*, 541–550. https://doi.org/10.1038/s41592-020-0799-7.
32. Brichacek, A.L., Benkovic, S.A., Chakraborty, S., Nwafor, D.C., Wang, W., Jun, S., Dakhlallah, D., Geldenhuys, W.J., Pinkerton, A.B., Millán, J.L., et al. (2019). Systemic inhibition of tissue-nonspecific alkaline phosphatase alters the brain-immune axis in experimental sepsis. Sci. Rep. *9*, 18788. https://doi.org/10.1038/s41598-019-55154-2.
33. Smith, L.K., Verovskaya, E., Bieri, G., Horowitz, A.M., von Ungern-Sternberg, S.N.I., Lin, K., Seizer, P., Passegué, E., and Villeda, S.A. (2020). The aged hematopoietic system promotes hippocampal-dependent cognitive decline. Aging Cell *19*, e13192. https://doi.org/10.1111/acel.13192.
34. Nakada-Honda, N., Cui, D., Matsuda, S., and Ikeda, E. (2021). Intravenous injection of cyclophilin A realizes the transient and reversible opening of barrier of neural vasculature through basigin in endothelial cells. Sci. Rep. *11*, 19391. https://doi.org/10.1038/s41598-021-98163-w.
35. Katsimpardi, L., Litterman, N.K., Schein, P.A., Miller, C.M., Loffredo, F.S., Wojtkiewicz, G.R., Chen, J.W., Lee, R.T., Wagers, A.J., and Rubin, L.L. (2014). Vascular and Neurogenic Rejuvenation of the Aging Mouse Brain by Young Systemic Factors. Science *344*, 630–634. https://doi.org/10.1126/science.1251141.
36. Stephan, A.H., Madison, D.V., Mateos, J.M., Fraser, D.A., Lovelett, E.A., Coutellier, L., Kim, L., Tsai, H.-H., Huang, E.J., Rowitch, D.H., et al. (2013). A Dramatic Increase of C1q Protein in the CNS during Normal

Aging. J. Neurosci. *33*, 13460–13474. https://doi.org/10.1523/jneurosci.1333-13.2013.

37. Hou, Y., Dan, X., Babbar, M., Wei, Y., Hasselbalch, S.G., Croteau, D.L., and Bohr, V.A. (2019). Ageing as a risk factor for neurodegenerative disease. Nat. Rev. Neurol. *15*, 565–581. https://doi.org/10.1038/s41582-019-0244-7.

38. Oakley, H., Cole, S.L., Logan, S., Maus, E., Shao, P., Craft, J., Guillozet-Bongaarts, A., Ohno, M., Disterhoft, J., Van Eldik, L.V., et al. (2006). Intraneuronal beta-amyloid aggregates, neurodegeneration, and neuron loss in transgenic mice with five familial Alzheimer's disease mutations: potential factors in amyloid plaque formation. J. Neurosci. *26*, 10129–10140. https://doi.org/10.1523/jneurosci.1202-06.2006.

39. Kimura, R., and Ohno, M. (2008). Impairments in remote memory stabilization precede hippocampal synaptic and cognitive failures in 5XFAD Alzheimer mouse model. Neurobiol. Dis. *33*, 229–235. https://doi.org/10.1016/j.nbd.2008.10.006.

40. Maguire, G.A., and Gossner, A. (1995). Glycosyl Phosphatidyl Inositol Phospholipase D Activity in Human Serum. Ann. Clin. Biochem. *32*, 74–78. https://doi.org/10.1177/000456329503200107.

41. Keren-Shaul, H., Spinrad, A., Weiner, A., Matcovitch-Natan, O., Dvir-Szternfeld, R., Ulland, T.K., David, E., Baruch, K., Lara-Astaiso, D., Toth, B., et al. (2017). A Unique Microglia Type Associated with Restricting Development of Alzheimer's Disease. Cell *169*, 1276–1290.e17. https://doi.org/10.1016/j.cell.2017.05.018.

42. Ungvari, Z., Tarantini, S., Kiss, T., Wren, J.D., Giles, C.B., Griffin, C.T., Murfee, W.L., Pacher, P., and Csiszar, A. (2018). Endothelial dysfunction and angiogenesis impairment in the ageing vasculature. Nat. Rev. Cardiol. *15*, 555–565. https://doi.org/10.1038/s41569-018-0030-z.

43. Zlokovic, B.V. (2011). Neurovascular pathways to neurodegeneration in Alzheimer's disease and other disorders. Nat. Rev. Neurosci. *12*, 723–738. https://doi.org/10.1038/nrn3114.

44. Nation, D.A., Sweeney, M.D., Montagne, A., Sagare, A.P., D'Orazio, L.M., Pachicano, M., Sepehrband, F., Nelson, A.R., Buennagel, D.P., Harrington, M.G., et al. (2019). Blood-brain barrier breakdown is an early biomarker of human cognitive dysfunction. Nat. Med. *25*, 270–276. https://doi.org/10.1038/s41591-018-0297-y.

45. Sweeney, M.D., Sagare, A.P., and Zlokovic, B.V. (2018). Blood–brain barrier breakdown in Alzheimer disease and other neurodegenerative disorders. Nat. Rev. Neurol. *14*, 133–150. https://doi.org/10.1038/nrneurol.2017.188.

46. Arvanitakis, Z., Capuano, A.W., Leurgans, S.E., Bennett, D.A., and Schneider, J.A. (2016). Relation of cerebral vessel disease to Alzheimer's disease dementia and cognitive function in elderly people: a cross-sectional study. Lancet Neurol. *15*, 934–943. https://doi.org/10.1016/s1474-4422(16)30029-1.

47. Lee, S., Viqar, F., Zimmerman, M.E., Narkhede, A., Tosto, G., Benzinger, T.L.S., Marcus, D.S., Fagan, A.M., Goate, A., Fox, N.C., et al. (2016). White matter hyperintensities are a core feature of Alzheimer's disease: Evidence from the dominantly inherited Alzheimer network. Ann. Neurol. *79*, 929–939. https://doi.org/10.1002/ana.24647.

48. Ozek, C., Krolewski, R.C., Buchanan, S.M., and Rubin, L.L. (2018). Growth Differentiation Factor 11 treatment leads to neuronal and vascular improvements in the hippocampus of aged mice. Sci. Rep. *8*, 17293. https://doi.org/10.1038/s41598-018-35716-6.

49. Park, M.H., Lee, J.Y., Park, K.H., Jung, I.K., Kim, K.-T., Lee, Y.-S., Ryu, H.-H., Jeong, Y., Kang, M., Schwaninger, M., et al. (2018). Vascular and Neurogenic Rejuvenation in Aging Mice by Modulation of ASM. Neuron *100*, 762. https://doi.org/10.1016/j.neuron.2018.10.038.

50. Leiter, O., Brici, D., Fletcher, S.J., Yong, X.L.H., Widagdo, J., Matigian, N., Schroer, A.B., Bieri, G., Blackmore, D.G., Bartlett, P.F., et al. (2023). Platelet-derived exerkine CXCL4/platelet factor 4 rejuvenates hippocampal neurogenesis and restores cognitive function in aged mice. Nat. Commun. *14*, 4375. https://doi.org/10.1038/s41467-023-39873-9.

51. Leiter, O., Zhuo, Z., Rust, R., Wasielewska, J.M., Grönnert, L., Kowal, S., Overall, R.W., Adusumilli, V.S., Blackmore, D.G., Southon, A., et al. (2023). Selenium mediates exercise-induced adult neurogenesis and reverses learning deficits induced by hippocampal injury and aging. Cell Metab. *35*, 1085. https://doi.org/10.1016/j.cmet.2023.04.019.

52. Lourenco, M.V., Frozza, R.L., de Freitas, G.B., Zhang, H., Kincheski, G.C., Ribeiro, F.C., Gonçalves, R.A., Clarke, J.R., Beckman, D., Staniszewski, A., et al. (2019). Exercise-linked FNDC5/irisin rescues synaptic plasticity and memory defects in Alzheimer's models. Nat. Med. *25*, 165–175. https://doi.org/10.1038/s41591-018-0275-4.

53. Islam, M.R., Valaris, S., Young, M.F., Haley, E.B., Luo, R., Bond, S.F., Mazuera, S., Kitchen, R.R., Caldarone, B.J., Bettio, L.E.B., et al. (2021). Exercise hormone irisin is a critical regulator of cognitive function. Nat. Metab. *3*, 1058–1070. https://doi.org/10.1038/s42255-021-00438-z.

54. Trejo, J.L., Carro, E., and Torres-Aleman, I. (2001). Circulating insulin-like growth factor I mediates exercise-induced increases in the number of new neurons in the adult hippocampus. J. Neurosci. *21*, 1628–1634. https://doi.org/10.1523/JNEUROSCI.21-05-01628.2001.

55. Schroer, A.B., Ventura, P.B., Sucharov, J., Misra, R., Chui, M.K.K., Bieri, G., Horowitz, A.M., Smith, L.K., Encabo, K., Tenggara, I., et al. (2023). Platelet factors attenuate inflammation and rescue cognition in ageing. Nature *620*, 1071–1079. https://doi.org/10.1038/s41586-023-06436-3.

56. Park, C., Hahn, O., Gupta, S., Moreno, A.J., Marino, F., Kedir, B., Wang, D., Villeda, S.A., Wyss-Coray, T., and Dubal, D.B. (2023). Platelet factors are induced by longevity factor klotho and enhance cognition in young and aging mice. Nat. Aging *3*, 1067–1078. https://doi.org/10.1038/s43587-023-00468-0.

57. Oh, H.S.-H., Rutledge, J., Nachun, D., Pálovics, R., Abiose, O., Moran-Losada, P., Channappa, D., Urey, D.Y., Kim, K., Sung, Y.J., et al. (2023). Organ aging signatures in the plasma proteome track health and disease. Nature *624*, 164–172. https://doi.org/10.1038/s41586-023-06802-1.

58. Li, X., Shi, X., McPherson, M., Hager, M., Garcia, G.G., and Miller, R.A. (2022). Cap-independent translation of GPLD1 enhances markers of brain health in long-lived mutant and drug-treated mice. Aging Cell *21*, e13685. https://doi.org/10.1111/acel.13685.

59. Li, X., Hager, M., McPherson, M., Lee, M., Hagalwadi, R., Skinner, M.E., Lombard, D., and Miller, R.A. (2023). Recapitulation of anti-aging phenotypes by global, but not by muscle-specific, deletion of PAPP-A in mice. GeroScience *45*, 931–948. https://doi.org/10.1007/s11357-022-00692-3.

60. Hager, M., Chang, P., Lee, M., Burns, C.M., Endicott, S.J., Miller, R.A., and Li, X. (2024). Recapitulation of anti-aging phenotypes by global overexpression of PTEN in mice. GeroScience *46*, 2653–2670. https://doi.org/10.1007/s11357-023-01025-8.

61. Thrupp, N., Frigerio, C.S., Wolfs, L., Skene, N.G., Fattorelli, N., Poovathingal, S., Fourne, Y., Matthews, P.M., Theys, T., Mancuso, R., et al. (2020). Single-Nucleus RNA-Seq Is Not Suitable for Detection of Microglial Activation Genes in Humans. Cell Rep. *32*, 108189. https://doi.org/10.1016/j.celrep.2020.108189.

62. Chan, K.Y., Jang, M.J., Yoo, B.B., Greenbaum, A., Ravi, N., Wu, W.-L., Sánchez-Guardado, L., Lois, C., Mazmanian, S.K., Deverman, B.E., et al. (2017). Engineered AAVs for efficient noninvasive gene delivery to the central and peripheral nervous systems. Nat. Neurosci. *20*, 1172–1179. https://doi.org/10.1038/nn.4593.

63. Aurnhammer, C., Haase, M., Muether, N., Hausl, M., Rauschhuber, C., Huber, I., Nitschko, H., Busch, U., Sing, A., Ehrhardt, A., et al. (2012). Universal Real-Time PCR for the Detection and Quantification of Adeno-Associated Virus Serotype 2-Derived Inverted Terminal Repeat Sequences. Hum. Gene Ther. Methods *23*, 18–28. https://doi.org/10.1089/hgtb.2011.034.

64. Sanjana, N.E., Shalem, O., and Zhang, F. (2014). Improved vectors and genome-wide libraries for CRISPR screening. Nat. Methods *11*, 783–784. https://doi.org/10.1038/nmeth.3047.

65. Alamed, J., Wilcock, D.M., Diamond, D.M., Gordon, M.N., and Morgan, D. (2006). Two-day radial-arm water maze learning and memory task; robust

resolution of amyloid-related memory deficits in transgenic mice. Nat. Protoc. *1*, 1671–1679. https://doi.org/10.1038/nprot.2006.275.

66. Stevenson, M.E., Bieri, G., Kaletsky, R., St Ange, J.St., Remesal, L., Pratt, K.J.B., Zhou, S., Weng, Y., Murphy, C.T., and Villeda, S.A. (2023). Neuronal activation of Gαq EGL-30/GNAQ late in life rejuvenates cognition across species. Cell Rep. *42*, 113151. https://doi.org/10.1016/j.celrep.2023.113151.

67. Crouch, E.E., and Doetsch, F. (2018). FACS isolation of endothelial cells and pericytes from mouse brain microregions. Nat. Protoc. *13*, 738–751. https://doi.org/10.1038/nprot.2017.158.

68. Sasmita, A.O., Ong, E.C., Nazarenko, T., Mao, S., Komarek, L., Thalmann, M., Hantakova, V., Spieth, L., Berghoff, S.A., Barr, H.J., et al. (2025). Parental origin of transgene modulates amyloid-β plaque burden in the 5xFAD mouse model of Alzheimer's disease. Neuron *113*, 838–846.e4. https://doi.org/10.1016/j.neuron.2024.12.025.

69. Bieri, G., Lucin, K.M., O'Brien, C.E., Zhang, H., Villeda, S.A., and Wyss-Coray, T. (2018). Proteolytic cleavage of Beclin 1 exacerbates neurodegeneration. Mol. Neurodegener. *13*, 68. https://doi.org/10.1186/s13024-018-0302-4.

70. Lin, K., Bieri, G., Gontier, G., Müller, S., Smith, L.K., Snethlage, C.E., White, C.W., Maybury-Lewis, S.Y., and Villeda, S.A. (2021). MHC class I H2-Kb negatively regulates neural progenitor cell proliferation by inhibiting FGFR signaling. PLoS Biol. *19*, e3001311. https://doi.org/10.1371/journal.pbio.3001311.

Please cite this article in press as: Bieri et al., Liver exerkine reverses aging- and Alzheimer's-related memory loss via vasculature, Cell (2026), https://doi.org/10.1016/j.cell.2026.01.024

CellPress
OPEN ACCESS

STAR★METHODS

KEY RESOURCES TABLE

REAGENT or RESOURCE	SOURCE	IDENTIFIER
Antibodies		
Rabbit polyclonal anti ALPL	R&D Systems	Cat#AF2910; RRID: AB_664062
Mouse monoclonal anti ALPL	R&D Systems	Cat#MAB29092; RRID: AB_2924405
Rat monoclonal anti CD31 (PECAM-1)	BioLegend	Cat#160202; RRID: AB_2876566
Goat polyclonal anti CD31 (PECAM-1)	R&D System	Cat#AF3628; RRID: AB_2161028
Rabbit polyclonal anti AQP4	Millipore	Cat#AB2218; RRID: AB_11210366
Rabbit monoclonal anti AQP4 [D1F8E]	Cell Signal Technology	Cat#59678; RRID: AB_2799571
Mouse monoclonal anti-β-Amyloid, 1-16 Antibody [6E10]	BioLegend	Cat#803001; RRID: AB_2564653
Mouse monoclonal anti Gapdh [6C5]	Abcam	Cat#ab8245; RRID: AB_2107448
Mouse monoclonal anti beta Actin-HRP [AC-15]	Abcam	Cat#ab49900; RRID: AB_867494
Rabbit monoclonal anti Caveolin1 (Cav1)	Cell Signal Technology	Cat#3267; RRID: AB_2275453
Rabbit monoclonal anti C1q	Abcam	Cat#ab182451; RRID: AB_2732849
Rabbit polyclonal anti GFAP	Dako	Cat#Z0334; RRID: AB_10013382
Rabbit monoclonal anti DCX	Cell Signal Technology	Cat#40619; RRID: AB_3696702
Mouse monoclonal anti MCM2/BM28	BD Biosciences	Cat#610700; RRID: AB_2141952
Guinea Pig polyclonal anti full length (FL) APP	Synaptic Systems	Cat#127 005; RRID: AB_2832229
Mouse monoclonal anti Beta-secretase 1 (BACE1) (3D5)	Sigma-Aldrich/Millipore	Cat#MABN2640; RRID: AB_3738362
Rabbit monoclonal anti PS1	Cell Signal Technology	Cat#5643S; RRID: AB_10706356
Mouse monoclonal anti BIII-Tubulin/TUBB3	BioLegend	Cat# 801201; RRID: AB_2313773
Rat anti CD16/32	BD Biosciences	Cat#553142; RRID: AB_394657
Rat anti CD45-PE	BD Biosciences	Cat#553081; RRID: AB_394611
Rat anti CD41-PE	BD Biosciences	Cat#558040; RRID: AB_397004
Rat anti CD31-APC	BD Biosciences	Cat#551262; RRID: AB_398497
Bacterial and virus strains		
NEB® 5-alpha Competent *E. coli*	New England Biolabs (NEB)	Cat#C2987U
Biological samples		
Mouse brain tissue	This paper	N/A
Mouse liver tissue	This paper	N/A
Human cortex tissue block	This paper	N/A
Chemicals, peptides, and recombinant proteins		
SBI-425	Sigma-Aldrich; Cayman Chemicals	Cat#SML2935; Cat#34626
PEI	Polysciences	Cat#23966-1
Hoechst 33342	Thermo Fisher	Cat#H3570
Thioflavine S	Sigma/Millipore	Cat#T1892-25G
EZ-Link™ Sulfo-NHS-LC-Biotin	Thermo Fisher	Cat#21335
Atto 647N NHS ester	Sigma-Aldrich	Cat#18373-1MG-F
Holo-Transferrin	Sigma-Aldrich	Cat#T4132
Streptavidin-AlexaFluor647	Thermo Fisher	Cat#S32357
Percoll solution	Cytiva	Cat#17089101
TrueBlack	Biotium	Cat#23007
Critical commercial assays		
Vector® Red Substrate Kit, Alkaline Phosphatase	Vector Laboratories	Cat#SK-5100
SEAP Reporter Gene Assay Kit	Abcam	Cat#ab133077
NEBuilder HiFi DNA Assembly Kit	NEB	Cat#E5520S

(*Continued on next page*)

Please cite this article in press as: Bieri et al., Liver exerkine reverses aging- and Alzheimer's-related memory loss via vasculature, Cell (2026), https://doi.org/10.1016/j.cell.2026.01.024

Continued

REAGENT or RESOURCE	SOURCE	IDENTIFIER
PureLink RNA Mini kit	Thermo Fisher	Cat#12183025
Direct-zol™ RNA Purification Kit, Miniprep Plus	Zymo Research	Cat#R2072
High Capacity cDNA Reverse Transcription kit	Thermo Fisher	Cat#4374966
PowerUp SYBR Green Master Mix	Thermo Fisher	Cat#A25742
Zeba™ Spin Desalting Columns, 7K MWCO, 5 mL	Thermo Fisher	Cat#89892
Miltenyi Neural Dissociation Kits (P)	Miltenyi	Cat#130-092-628
Deposited data		
Single-nucleus RNA sequencing data	This paper	GEO: GSE304483
BEC single-cell RNA sequencing data	This paper	GEO: GSE269061
Experimental models: Cell lines		
293T	ATCC	Cat#CRL-3216; RRID: CVCL_0063
Neuro-2a	ATCC	Cat#CCL-131; RRID: CVCL_0470
Experimental models: Organisms/strains		
C57BL/6J	The Jackson Laboratory	Strain#000664
C57BlL6/J NIA Aging mouse colony	NIA	N/A
5xFAD (B6SJL-Tg(APPSwFlLon, PSEN1*M146L*L286V)6799Vas/Mmjax)	The Jackson Laboratory/ MMRRC	MMRRC Strain#034840-JAX
B6;129-Gt(ROSA) 26Sor$^{tm1(CAG-cas9*,-EGFP)Fezh}$/J	The Jackson Laboratory	Strain#024857
Oligonucleotides		
Gpld1 qPCR FWD: GGAAGCAGAGAGGAATTGTGGC	Horowitz et al.[16]	N/A
Gpld1 qPCR REV: TCCAAACCACGAGAAGTCCTCC	Horowitz et al.[16]	N/A
Gapdh qPCR FWD: GGGTGTGAACCACGAGAAAT	This paper	N/A
Gapdh qPCR REV: ACTGTGGTCATGAGCCCTTC	This paper	N/A
GPLD1 qPCR FWD (human)	This paper	N/A
GPLD1 qPCR REV (human)	This paper	N/A
Alpl qPCR FWD: GAACAGACCCTCCCCACGAG	This paper	N/A
Alpl qPCR REV: GTGCCGATGGCCAGTACTAA	This paper	N/A
Alpl qPCR FWD2: TAACACCAACGCTCAGGTCC	This paper	N/A
Alpl qPCR REV2: TGGATGTGACCTCATTGCCC	This paper	N/A
Recombinant DNA		
pAAV2/8	Addgene	Plasmid#112864
pUCmini-iCAP-PHP.V1	Addgene	Plasmid#127847
pAAV-CAG-mRuby2	Addgene	Plasmid#99123
pEMS1938	Addgene	Plasmid#82563
pAdDeltaF6	Addgene	Plasmid#112867
pMD2.G	Addgene	Plasmid#12259
psPAX2	Addgene	Plasmid#12260
lentiCRISPR v2	Addgene	Plasmid#52961
pTB CMV Gpld1 IRES eGFP	Horowitz et al.[16]	N/A
pTB CMV Gpld1 H133N IRES eGFP	Horowitz et al.[16]	N/A
pTB CMV Gpld1 H158N IRES eGFP	Horowitz et al.[16]	N/A
pTB CMV IRES eGFP	Horowitz et al.[16]	N/A
pTB CMV Alpl IRES eGFP	This paper	N/A
pTB CMV GPLD1 (human) IRES eGFP	This paper	N/A
pAAV-CAG-Alpl	This paper	N/A
pAAV-CRE-hU6-gRNA	This paper	N/A
pAAV TBG eGFP	This paper	N/A

(*Continued on next page*)

Please cite this article in press as: Bieri et al., Liver exerkine reverses aging- and Alzheimer's-related memory loss via vasculature, Cell (2026), https://doi.org/10.1016/j.cell.2026.01.024

Continued

REAGENT or RESOURCE	SOURCE	IDENTIFIER
pAAV TBG Gpld1	This paper	N/A
pAAV TBG Gpld1 H133N	This paper	N/A
Software and algorithms		
FIJI/ImageJ2	ImageJ	https://imagej.net/software/fiji/
Prism 10	GraphPad	https://www.graphpad.com
Zeiss Zen 3.7/3.3	Zeiss	N/A
Cell Ranger version 7.1.0.	10X Genomics	https://support.10xgenomics.com/single-cell-gene-expression/software/downloads/latest
RStudio	Posit	https://posit.co/downloads/
Seurat v5	Satija Lab	https://satijalab.org/seurat/
Wheel Manager Software	MedAssociates	Cat# SOF-860
Smart Video Tracking Software	Panlab/Harvard Apparatus	http://www.panlab.com/en/products/smart-video-tracking-software-panlab
ChemiDoc Image Lab Software 6.1	BioRad	N/A
EthoVision XT	Noldus	N/A

EXPERIMENTAL MODEL AND STUDY PARTICIPANT DETAILS

Mouse strains

The following mouse lines were used: C57BL/6J mice (Jackson Laboratory, strain # 000664), C57BL/6J aged mice (National Institutes of Aging), B6SJL-Tg(APPSwFILon,PSEN1*M146L*L286V)6799Vas/Mmjax (5xFAD; Jackson Laboratory/MMRRC strain # 034840-JAX) and homozygous inducible Cas9 transgenic mice (B6;129-*Gt(ROSA)26Sor*$^{tm1(CAG-cas9*,-EGFP)Fezh}$/J; Jackson Laboratory strain# 034840-JAX). All studies in wildtype C57Bl6 mice were done in young (3-6 month) or aged (18-24 month) mice. Young wildtype mice were acquired at 8 weeks and aged in-house under standard housing conditions. Male 5xFAD and WT littermate controls were acquired at 6 weeks and aged in house or 5xFAD transgenic males were bred with wildtype female mice and aged in-house. 5xFAD mice were treated at 6-9 month with GPLD1 and 8-11 month with TNAP inhibitor followed by behavioral testing. Male homozygous Cas9 mice were bred and aged in-house and used for experimental purposes at 20-22 months. All sequencing studies were performed with male mice. For each age group and experiment, litter mates were randomly assigned to each treatment group. Mice were group housed until 7-10 days before the start of behavioral testing. Extra enrichment was added during single housing. Health was regularly assessed, and mice were weighed during the course of treatments and testing. The numbers of mice used to result in statistically significant differences were calculated using standard power calculations with a = 0.05 and a power of 0.8. We used an online tool to calculate power (https://www.stat.uiowa.edu/~rlenth/Power/index.html) and samples size based on experience with the respective tests, variability of the assays and inter-individual differences within groups. Mice were housed under specific pathogen-free conditions under a 12h light-dark cycle, and all animal handling and use was in accordance with institutional guidelines approved by the University of California San Francisco Institutional Animal Care and Use Committee (IACUC).

Human tissue

Post-mortem brain tissues from young, confirmed AD and age-matched, non-demented, non-pathological controls were obtained from Duke ADRC in strict accordance with all ethical and institutional guidelines. Individuals were grouped by age and clinical diagnosis. All subjects were male and Caucasian. Autopsy brain tissue from the frontal cortex of 6 young donors, non-demented aged and neuropathologically confirmed AD case were studied. Age at death: Young: 27+/-5.2; Aged: 81+/-12; 85+/-6.6 years. The aged group had a mean MMSE score of 29+/-1.4, while AD was 18.17+/-5. The AD neuropathological changes in the AD group where classified as intermediate to high, with a Braak stage of III-V. Additional details in Table S1.

Cell lines

293T and Neuro-2a cells were cultured under standard conditions using DMEM with 10% FBS in 37C incubators with 5% CO2.

Please cite this article in press as: Bieri et al., Liver exerkine reverses aging- and Alzheimer's-related memory loss via vasculature, Cell (2026), https://doi.org/10.1016/j.cell.2026.01.024

METHOD DETAILS

Exercise intervention

Exercised mice were single-housed and given continuous access to a running wheel (Med Associates Inc., Cat# ENV-047) in their home cage for 6 weeks. Distance ran per mouse was tracked using Wheel Manager software (Med Associates, Inc.). Sedentary control mice were single-housed and given a locked wheel, house and nestlet as alternative enrichments.

Liver GPLD1 expression

GPLD1, catalytically inactive GPLD1 with a H133N amino acid substitution (H133N), or GFP control were overexpressed in the liver *in vivo* using a hydrodynamic tail vein injection or AAV-delivery approach. For hydrodynamic tail vein injections, endotoxin-free plasmids were prepared using an endotoxin-free Maxi-Prep Kit. All plasmid sequences were verified by whole plasmid sequencing and low endotoxin level validated prior to administration (Thermo Fisher cat# PIA39552). Mice were briefly placed in a restrainer and GPLD1, H133N or GFP plasmid DNA (50ug) was suspended in 3mL sterile saline and injected in the tail vein in 5-7 seconds. Alternatively, GPLD1, H133N or GFP were expressed using an AAV-based expression plasmid with a hepatocyte specific TBG promoter and packaged with the AAV8 capsid. Genomic titers were assessed using qPCR with ITR specific primers as viral genomes per volume (vg/mL). 10 ^15 vg/kg were injected retro-orbitally into each mouse.

TNAP inhibition

The orally bioavailable TNAP inhibitor SBI-425 was sourced from Sigma-Aldrich (Cat# SML2935) and Cayman Chemicals (Cat# 34626). TNAP inhibitor and control chow were manufactured by Research Diets Inc using the open standard diet (Cat# D11112201) with a formulation of 200mg/kg SBI-425. All mice had ad libitum access to the chow.

AAV production

AAV GPLD1, H133N and GFP plasmids were generated using the NEBuilder HiFi DNA Assembly Kit (NEB #E5520S), following the manufacturer's recommended design considerations and protocol. Briefly, the AAV2 vector backbone containing a TBG promoter was digested with the restriction enzymes NotI and HindIII and gel purified. eGFP and murine GPLD1 coding sequences were PCR-amplified with primer sets that included a 20 nucleotide overlap with the backbone and preserved the restriction sites. The H133N mutation in GPLD1 was introduced using the QuikChange Lightning Site-directed Mutagenesis kit (Agilent Cat# 210518) in combination with the following mutagenesis primers: GCTGACGTGAGCTGGAATAGCCTGG GTATTG, CAATACCCAGGCTATTCCAGC TCACGTCAGC.

The TNAP/Alpl expressing AAV construct was based on the control pAAV-CAG-Ruby2 plasmid (a gift from Viviana Gradinaru; Addgene plasmid #99123)[62] and pEMS1938 plasmid with the Ple261 promoter (a gift from E. Simpson; Addgene plasmid# 82563). The Alpl mRNA with partial 3' and 5' UTRs was PCR-amplified from a mouse hippocampal cDNA library and cloned using the pENTER/D-TOPO cloning kit (Thermo Fischer Scientific K240020). The Alpl coding sequence was further amplified with primers containing the restriction sites KpnI and EcoRI. Both Alpl and the AAV backbone were digested with KpnI and EcoRI followed by ligation. All plasmids were sequence-verified using whole-plasmid sequencing (Primordium Labs).

For large scale AAV production HEK293T cells were cultured in 10x T182 flasks per virus. HEK293T cells were transfected with PEI (1mg/mL; Polysciences Cat# 23966-1), a combination of the AAV backbone, capsid and helper plasmid and Opti-MEM (Thermo Fisher Scientific Cat# 31985-062). For liver-targeting viruses, the pAAV2/8 capsid was used (a gift from James M. Wilson; Addgene plasmid# 112864) and for the BEC-targeting viruses the PHP.V1 capsid was used (pUCmini-iCAP-PHP.V1 was a gift from Viviana Gradinaru; Addgene plasmid# 127847).[31] Media change was performed after overnight incubation. Supernatant and cells were harvested after 72-96 hours for AAV viral particle isolation and concentration. Briefly, cells were mechanically detached and collected together with the viral particle containing culture media. The media was collected after 10 minute centrifugation at 1000g and the remaining pellet was resuspended in chilled PBS. Following 4 freeze-thaw cycles, the lysate was cleared using centrifugation at 10000g for 10 minutes. The supernatant was re-combined with the cell culture media and filtered through 0.45μm PES filter. AAV viral particles were purified and concentrated using Ultracentrifugation (Beckman Coulter). Genomic viral titers were measured using qPCR in combination with primer sets targeting the ITR sequence (FWD: GGAACCCCTAGTGATGGAGTT; REV CGGCC TCAGTGAGCGA).[63]

Abrogation of cerebrovascular TNAP in aged Cas9-inducible mice

5 different Alpl-targeting gRNAs and a non-targeting safe harbor control guide were first cloned into the lentiCRISPRv2 plasmid (lentiCRISPR v2 was a gift from Feng Zhang; Addgene plasmid #52961),[64] packaged into lentiviral particles and used to transduce murine Neuro-2a cells. One week after puromycin selection (72 hours) and recovery, Alpl expression was assessed using RT-qPCR analysis. The U6 gRNA cassettes of Alpl gRNA1 (target sequence: ACGCGATGCAACACCACTCAGGG) and the control guide were then cloned into an AAV backbone expressing a CAG-CRE. AAV particles were packaged with BEC-targeting PhP.V1 capsid and administered retro-orbitally into aged transgenic mice (20-22 months) with a stop-lox-stop Cas9 transgene (JAX strain# 024857). Genomic

Please cite this article in press as: Bieri et al., Liver exerkine reverses aging- and Alzheimer's-related memory loss via vasculature, Cell (2026), https://doi.org/10.1016/j.cell.2026.01.024

titers were assessed using qPCR with ITR specific primers as viral genomes per volume (vg/mL). 10 ^15 vg/kg were injected retro-orbitally into each mouse. NHS-biotin, labelled Transferring, AP activity measurements and behavioral testing were performed 5-8 weeks after AAV administration.

Novel object recognition (NOR)

The NOR task was performed using an established protocol.[7] Specifically, on day one (the habituation phase), mice performed open field testing by exploring an empty arena (40cm x 40cm) for 10 min. Infrared photobeam breaks were recorded and movement metrics were analyzed using the MotorMonitor software (Kinder Scientific). On day two (the training phase), two identical objects were placed into the habituated arena, and the mice were allowed to explore for 5 min. On day three (the testing phase), one object was replaced with a novel object, and the mice were allowed to explore for 5 min. The time spent exploring each object was quantified using the Smart Video Tracking Software (Panlab; Harvard Apparatus). Two different sets of objects were used. To control for any inherent object preference, half of the mice were exposed to object A as their novel object and half to object B. To control for any potential object-independent location preference, the location of the novel object relative to the trained object was also counterbalanced. To determine the percentage of time with the novel object, we calculate (time with novel object)/(time with trained object + time with novel object) $\times$ 100. Mice that did not explore both objects during the training phase were excluded from the analysis.

Radial arm water maze (RAWM)

Spatial learning and memory were assessed using an established 8-arm radial water maze paradigm.[65] In this task, the mouse was trained to the location of a constant goal arm throughout the training and testing phase. The start arm changed each trial. Entry into an incorrect arm was scored as an error, and errors were averaged over training blocks consisting of three consecutive trials. During training (day 1), the mice were trained for 12 trials (blocks 1–4), with trials alternating between a visible and hidden platform. After an hour break, learning was tested for 3 trials (block 5) using only a hidden platform. During testing (day 2), the mice were tested for 15 trials (blocks 6–10) with a hidden platform. When scoring, investigators were blinded to treatment and genotype.

Y-maze

The Y-maze task was conducted using an established forced alternation protocol. During the training phase, mice were placed in the start arm facing the wall and allowed to explore the start and trained arm for 5 minutes, while entry to the 3rd arm (novel arm) was blocked. The maze was cleaned between each mouse to remove odor cues, and the trained arm was alternated between mice. The mouse was then returned to its home cage. After 30-45 minutes, the mouse was placed in the start arm and allowed to explore all 3 arms for 5 minutes. Time spent in each arm was quantified using the Smart Video Tracking Software (Panlab; Harvard Apparatus). Percent time in each arm was defined as time in arm divided by time spent in all arms during the first minute of the task. The learning index was calculated as (entries in novel arm - entries in familiar arm)/(entries in novel arm + entries in familiar arm).

Active Place Avoidance

The mice were placed in a rotating cylindrical arena (Maze Engineers; 1 meter in diameter, rotation speed at 1 rotation/minute) and had to learn to avoid a stationary 60° area (shock zone) using visual cues placed around the arena. During the habituation day, the mice were placed in the rotating arena for a duration of 5 minutes during which the shock zone was inactive. During testing, mice were placed in the in the area diagonally away from the shock zone and recorded for 10 min/day for a total of 4 consecutive days. Between animals, the arena was cleaned with 70% ethanol. Shocks were delivered at 0.5 mA if the mice entered the shock zone for a minimum of 1 second, with an inter-shock latency of 1.5s. Trials were recorded, analyzed and shocks administered using Noldus Ethovision XT. Number of entries/day into the shock zone, the number of administered shocks/day and the cumulative number of shocks over all trials were calculated for each animal.

Health metrics

The *nestlet* assay was assessed using a pre-defined scoring system.[66] Mice were provided with two pressed cotton nestlets and given up to 48 hours to build nests. Nest forming behavior was measured based on a nestlet score with a scoring system of 1 = no nest built and a score of 5 = an enclosed nest, as preciously described. For each mouse, the nesting scores were averaged from two separate experiments performed at a one-week interval.

Motor coordination was evaluated with the RotarRod test using a standard mouse *RotaRod* apparatus with a 1-inch diameter rotating cylinder (Harvard Apparatus, PanLab). On the training day, mice were first habituated on the still cylinder for 30 seconds and then trained at a constant speed (5 rpm) for 5 minutes. The next day (testing day), mice were placed on the rod at a constant rotation (4 rpm) for 10 seconds, followed by an acceleration from 4 to 40 rpm in 300 seconds. The latency to fall was recorded for each mouse on 3 trials with a 15-minute intertrial interval.

Grip Strength was measured for all 4 paws using a standard Grip strength test apparatus with a wire grid (Bioseb). Mice were held by the tail, lowered towards the apparatus, and allowed to grab the metal grid before being pulled back horizontally. The maximum force applied to the grid was recorded and averaged for 6 trials per mouse.

Please cite this article in press as: Bieri et al., Liver exerkine reverses aging- and Alzheimer's-related memory loss via vasculature, Cell (2026), https://doi.org/10.1016/j.cell.2026.01.024

Tissue collection

Mice were anesthetized with 87.5 mg per kg ketamine and 12.5 mg per kg xylazine and transcardially perfused with 25ml ice-cold phosphate-buffered saline. For brain tissue used in histological analysis of the brain vasculature, transcardial perfusion with 25ml PBS was followed with 25ml ice-cold 4% PFA. For a subset of PBS-perfused animals the liver, heart, kidney, spleen, lung and tibialis anterior muscle were dissected and snap frozen. To process the brains, the whole brain was sectioned in half along the sagittal plane. The hippocampus and cortex from one hemisphere were subdissected and snap-frozen and the other was postfixed in phosphate-buffered 4% paraformaldehyde, pH 7.4 at 4 °C for 48 h before cryoprotection with 30% sucrose.

Single nucleus RNA sequencing

Neuronal nuclei were isolated based on the demonstrated protocol by 10x Genomics with modifications and performed on nuclei isolated from two-four mice per group (pool of 2 mice/well – 1 well for 5xFAD experiment and H133N of Figure 5, 2 wells for GPLD1/TNAPi samples). Only male mice were used for snRNAseq analysis. Briefly, flash-frozen dissected hippocampi were dounce-homogenized (Wheaton, Cat# 357538) in 500μL of Nuclei EZ prep lysis buffer (Sigma-Aldrich, NUC101, 1x RNAse Inhibitor) with 20 strokes of the loose pestle and 20 strokes of the tight pestle. 500 μL of Nuclei EZ prep lysis buffer was added and samples incubated for 7 minutes on ice. Samples were filtered through a 40μm filter and centrifuged at 500 RCF for 5 min at 4°C. Samples were resuspended in 1ml of Wash Buffer (PBS, 1%BSA, 1xRNAse Inhibitor) and incubated for 5 min on ice. Samples were centrifuged at 500 RCF for 5 min at 4°C, supernatant was removed, and samples were resuspended in 400μL of Wash Buffer with 1:10,000 dilution of Hoescht 33342 and incubated for five minutes before filtering through a 35μm FACS tube filter and sorting. Nuclei were sorted on a BD FACSAria II with a 100μm nozzle and with a flow rate of 1–2.5. Nuclei were first gated by forward and side scatter, then gated for doublets with height and width. Nuclei that were Hoechst+ were sorted and samples were combined per group. Isolated nuclei were given to the UCSF-CoLab Genomics Core for preparation with the 10x Genomics Chromium Single Cell Expression Solution 3′ kit. The Genomics Core prepared cells for 10x Genomics Chromium single-cell capture. 30,000 nuclei were loaded per sample. cDNA libraries were prepared according to the standard 10x Genomics protocols. The final library pool was sequenced on the NovaSeq 6000 or the NovaSeq X 10B system at the UCSF CAT Core. The raw base sequence calls were demultiplexed into sample-specific cDNA files with bcl2fastq/mkfastq and converted to count matrices using Cell Ranger 7.1 (10x Genomics).

Brain endothelial cell isolation and single cell RNA sequencing

Hippocampal brain endothelial cells were isolated using enzymatic tissue dissociation and fluorescent activated cell sorting[67] and single cell analysis was performed on pooled hippocampal BECs from a pool of hippocampi from eight mice per group (Young Control, Aged control, Aged GPLD1- and TNAP inhibitor treated). Brain endothelial cells derived from male mice were used for scRNAseq analysis. Mice were anesthetized with 87.5 mg per kg ketamine and 12.5 mg per kg xylazine and transcardially perfused with 30ml ice-cold phosphate-buffered saline. The entire brain was removed, then the hippocampus was sub-dissected. Single-cell suspensions were generated by enzyme-mediated (papain) and mechanical dissociation using Miltenyi Neural Dissociation Kits (P) (Miltenyi, 130-092-628) according to the manufacturer's instructions. The papain dissociation was done at 37°C for 10 minutes with three trituration steps. All other processing steps were performed at 4°C. Myelin was depleted from the suspensions using 22% Percoll solution (Cytiva, 17089101). Cell Fc receptors were blocked using a purified anti-mouse CD16/32 antibody (BD Biosciences, 553142) and stained for 30 minutes at 4°C with CD45-PE (BD Biosciences, 553081), CD41-PE (BD Biosciences, 558040) and CD31-APC (BD Biosciences, 551262) and DAPI (Thermo Scientific, 62248 1:1000). Cells were sorted on a BD FACSAria Fusion with a 100 μm nozzle and with a flow rate of 1–2.5. Cells were first gated by forward and side scatter, then gated for doublets with area and height. Cells per sample that were DAPI-, CD45-, CD41-, CD31+ were collected for sequencing analysis. Isolated cells were given to the UCSF-CoLab Genomics Core for analysis with the 10x Genomics Chromium Single Cell Expression Solution 3′ kit. The Genomics Core prepared cells for 10x Genomics Chromium single-cell capture. 22,000-30,000 cells were loaded per sample. cDNA libraries were prepared according to the standard 10x Genomics protocols. The final library pool was sequenced on the NovaSeq 6000 or the NovaSeq X 10B system at the UCSF CAT Core. The raw base sequence calls were demultiplexed into sample-specific cDNA files with bcl2fastq/mkfastq and converted to count matrices using Cell Ranger 7.1 (10x Genomics).

Single-cell and single-nucleus RNA sequencing analysis

Raw FASTQ files were processed and aligned to mm10 using the Cell Ranger software package (10x Genomics) for the RNA expression matrix, including introns for single nucleus analysis. For the aging GPLD1/TNAP treatment, a total of 54,597 nuclei were sequenced at a depth of approximately 70,000 reads per cell and 60% sequencing saturation. For the 5xFAD sequencing, a total of 52,783 cells were sequenced at a depth of approximately 40,000 reads per cell and 31% sequencing saturation. Further QC and analysis were performed on R 4.2.2. For all experiments, downstream analysis and data visualization was performed using Seurat, as well as packages DropletUtils, ggplot2, knitr, WriteXLS, RColorBrewer, data.table, stringr, ggplot2, forcats, dplyr, Nebulosa, and htmlwidgets. Data were processed to remove doublets and unwanted sources of variation by removing nuclei with more than 6,000 and fewer than 200 genes per cell, number of counts more than 40,000 per nuclei, and regressing on number of UMIs. Genes expressed in fewer than three cells or nuclei were filtered out. Nuclei with a percentage of mitochondrial genes higher than 0.2% were removed. Final nuclei counts of 11062 (Aged CTRL), 20,713 (Aged GPLD1), 19581(Aged TNAP inhibitor), 17350 (WT GFP), 14404 (5xFAD GFP), and 18000 (5xFAD GPLD1) were used for gene expression analysis. Final cell count of 16594

Please cite this article in press as: Bieri et al., Liver exerkine reverses aging- and Alzheimer's-related memory loss via vasculature, Cell (2026), https://doi.org/10.1016/j.cell.2026.01.024

(Young Control BECs), 20576 (Aged Control BECs, 12605 (Aged GPLD1 BECs), 20892 (Aged TNAPi BECs). The matrices of data were log-normalized in a sparse data matrix, scaled, integrated with CCA integration, and PCA was applied to reduce dimensionality. The first 20 PCA components were used to cluster cells by Louvain clustering at a resolution of 0.4, implemented in Seurat while UMAP plots were independently generated to aid in 2D representation of multidimensional data independent of the clustering. Cell types were identified using known markers, as well as the Allen Mouse Brain Atlas,[4,5] and clusters containing more than one cell type specific marker were removed. Differential gene expression was performed on each cell type down-sampled to 800 nuclei/cluster/condition for the aging dataset, 550 nuclei/cluster/condition for the 5xFAD dataset, and 12,000 cells/condition for the BEC dataset. Differential gene expression was determined using MAST statistical testing with a minimum of 10% of nuclei expressed, log fold change threshold of 0.15, and a pseudocount of 0.01. Log-normalized gene expression data were used for visualizations with violin plots and UMAP feature plots. Average expression matrices were used for heatmap visualization. Volcano plots were created using the EnhancedVolcano package and UpSet plots with the ComplexHeatmap package.

RNA extraction, cDNA synthesis and RT-qPCR analysis

Total RNA was isolated from subdissected hippocampi, cortex, liver, kidney, spleen, lung, heart and tibialis anterior muscle tissue using TRI Reagent (Sigma-Aldrich, Cat#T9424) in combination with the PureLink RNA Mini Kit (Thermo Fisher Scientific Cat# 12183025) or Direct-zol™ RNA Purification Miniprep Plus Kit (Zymo Research Cat# R2072) following the manufacturer's protocol. 50-100mg tissue was dissociated using a Bead Ruptor Elite and Ceramic beads (Omni International Cat# 19-645-3). Lysates were centrifuged at 8,000 g for 10 min at 4 °C to remove cellular debris. Cell lines were lysed in the tissue culture plate using the Lysis reagent provided in the PureLink RNA Mini kit. The RNA concentrations were determined via Nanodrop and RNA was reverse-transcribed using the High-Capacity cDNA Reverse Transcription Kit (Thermo Fisher Scientific, Cat# 4368813). To quantify mRNA expression levels, equal amounts of cDNA were synthesized using the High-Capacity cDNA Reverse Transcription kit (ThermoFisher Scientific, Cat# 4368813), then mixed with SYBR Fast mix (Kapa Biosystems) and primers. Gapdh mRNA was amplified as an internal control. Quantitative RT-PCR was carried out in a CFX384 Real Time System (Bio-Rad). Each sample and primer set were run in triplicates and relative expression levels were calculated using the $2-\Delta\Delta ct$ method. The following primer sets were used:

Gapdh: GGGTGTGAACCACGAGAAAT, ACTGTGGTCATGAGCCCTTC
Gpld1: GGAAGCAGAGAGGAATTGTGGC, TCCAAACCACGAGAAGTCCTCC
Alpl Pair 1: GAACAGACCCTCCCCACGAG, GTGCCGATGGCCAGTACTAA
Alpl Pair 2: TAACACCAACGCTCAGGTCC, TGGATGTGACCTCATTGCCC

Western blot analysis

Brain tissue was lysed in chilled RIPA lysis buffer (Abcam Cat# ab156034) with complete protease inhibitor (Sigma-Aldrich Cat# 4693116001) and phosphatase inhibitor (Thermo-Fisher Cat# 78420). Tissue was dissociated using a Bead Ruptor Elite and Cermic beads (Omni International Cat# 19-645-3). Crude lysates were centrifuged at 10,000 g for 10 min at 4 °C to remove cellular debris. Protein concentrations in clarified lysates were quantified with a Pierce BCA protein assay. Tissue lysates were mixed with 4x NuPage LDS loading buffer (Invitrogen Cat# NP0008), loaded on a 4-12% SDS polyacrylamide gradient gel (BioRad Cat# 11346-02) and transferred onto a nitrocellulose or PVDF membrane using the Trans-Blot turbo transfer system (BioRad). For plasma samples, plasma was mixed with 4x NuPage LDS, water and 2-Mercaptoethanol and the 1 ul of plasma was loaded into each well. After transfer, some membranes were cut into strips at approximately 25kDa and 75kDa to probe for proteins with distinct molecular weight in parallel. The blots were blocked in 5% milk in Tris-Buffered Saline with 0.1% Tween (TBST) and incubated with anti-GAPDH (Abcam Cat# ab8245), anti-ALPL (R&D System Cat# MAB29092) and anti-ACTIN-Beta/ACTB (Abcam Cat# ab49900). APP protein and processing components were assessed using the following antibodies: anti-FL APP (Synaptic Systems Cat# 127 005), anti-APP 6E10 (human FL-APP and CTF detection; BioLegend Cat# 803001), anti-PS1 (Cell Signal Technology Cat# 5643S); anti-BACE1 (Sigma/Millipore Cat# MABN2640), anti-BIII-Tubulin (BioLegend Cat# 801201) primary antibodies.[68] Horseradish peroxidase-conjugated secondary antibodies and an ECL kit (BioRad Cat# 1705060) were used to detect protein signals. Membranes were imaged with a ChemiDoc Imaging System (BioRad). Selected images were exported and quantified using the built-in gel analysis tool in FIJI/ImageJ. GAPDH, ACTB and BIII-Tubulin bands were used for normalization.

Immunohistochemistry

Tissue processing and immunohistochemistry were performed on free-floating sections according to standard published techniques.[6] Cryoprotected brains were sectioned coronally at 40 μm with a freeze-stage microtome (Leica Camera). Free-floating sections were permeabilized with pre-treatment buffer (0.2% TritonX-100 in TBST) for 30 minutes, then washed 3x with TBST and blocked with TBST + 3% Normal Donkey serum (NDS). Sections were then incubated overnight at 4C with anti-ALPL (R&D Systems Cat# AF2910), anti-CD31 (BioLegend Cat# 160202 and R&D Systems Cat# AF3628), anti-AQP4 (Cell Signal cat# 59678S and Millipore cat# AB2218 or 59678S), anti-APP 6E10 (BioLegend Cat# 803001), anti-Caveolin1 (Cell Signal Technology Cat# 3267S) in TBST + 3% NDS. Labelling was revealed using secondary antibodies at 1:500 in TBST + 3% NDS for 1 hour room temperature. Nuclei were labelled with Hoechst (Thermo Fisher Scientific, Cat# H3570). Sections were mounted on Superfrost Plus microscopy slides and coverslipped with Prolong Gold. Sections were imaged using confocal microscopy (Zeiss LSM800 or Zeiss LSM900) or

bright-field microscopy (Keyence). Labelling intensity and thresholded areas were quantified and averaged for 3-5 hippocampal sections for each mouse using FIJI and Zeiss Zen image analysis tools.

Sulfo-NHS-biotin BBB leakage assay

Sulfo-NHS-LC-biotin (Thermo Fisher Cat# 21335) was reconstituted in sterile PBS pH7.4, stored on ice and used for up to 30 minutes before being discarded. Mice were injected retro-orbitally at a dose of 0.25mg/g BW (~7.5mg/mouse for a 30g mouse) and the biotin tracer was allowed to circulate for 5 min before perfusion and tissue collection. Mice were anesthetized with 87.5 mg per kg ketamine and 12.5 mg per kg xylazine and transcardially perfused with 25ml ice-cold PBS followed by 25ml 4% PFA. To process the brains, the whole brain was sectioned in half along the sagittal plane and postfixed in 4%PFA at 4 °C for 48 h before cryoprotection with 30% sucrose. Brains were then sectioned coronally at 40 μm with a freeze-stage microtome (Leica Camera) and stored in cryoprotective media. Brain sections were stained for vascular markers CD31 and AQP4 using standard immunohistochemistry approaches. A 1:1000 dilution of Streptavidin-AlexaFluor 647 was added during the secondary antibody incubation for 1 hour at room temperature. Sections were mounted on Superfrost Plus slides and coverslipped using ProlongGold. Hippocampal images were acquired using confocal microscopy (LSM900) and analyzed using Zeiss Zen software and ImageJ. Vascular area masks were generated by measuring the area covered by the vascular labelling. The NHS-biotin/Streptavidin labelling were measured, and the permeability index was determined as the area covered by NHS-biotin/Streptavidin signal outside of the vascular area mask.

Labelled Transferring (TF-647) uptake assay

50mg holo-Transferrin (Sigma Cat# T4132) was reconstituted in 4ml sterile PBS. Atto 647N NHS ester (Sigma Cat# 18373-1MG-F) was reconstituted in DMSO to generate a 30mM stock solution. Transferrin and Atto 647N NHS ester were mixed at a molar ratio of 1:1.8 and incubated at room temperature under constant agitation for 90 minutes. 50mM Tris (pH8) was added to quench the reaction and incubated at room temperature for 10 minutes. Reaction cleanup and unbound Atto 647N NHS ester was removed using two Zeba spin desalting columns (7k MWCO; Thermo Fisher Cat# 89892). 2 columns were used for each clean-up round. Protein concentration of the elution was determined using NanoDrop, adjusted to 10mg/ml in PBS and stored at -80C. Successful labeling was validated using Western blot analysis. 1μg of labelled and cold (unlabeled) Transferrin was separated on a 4-12% NuPAGE™ Bis-Tris Mini Protein Gel, transferred to a nitrocellulose membrane and fluorescent signal visualized using a ChemiDoc imager (BioRad). For *in vivo* Transferrin uptake assay, 1mg of labelled TF-647 was injected retro-orbitally 20h before tissue collection. Mice were anesthetized with 87.5 mg per kg ketamine and 12.5 mg per kg xylazine and transcardially perfused with 25ml ice-cold PBS followed by 25ml 4% PFA. Brains were postfixed in 4%PFA at 4 °C for 48 h before cryoprotection with 30% sucrose. Brains were then sectioned coronally at 40 μm with a freeze-stage microtome (Leica Camera) and stored in cryoprotective media. Brain sections were stained for vascular markers CD31 and AQP4 using standard immunohistochemistry approaches. Hippocampal images were acquired using confocal microscopy (LSM900 and LSM800) and analyzed using Zeiss Zen software and ImageJ. Vascular area masks were generated, and TF-647 intensity was selectively measured in the area occupied by vascular labeling in the hippocampus.

AP activity labelling

The Alkaline phosphatase activity labelling was performed on PFA-fixed free-floating sections (40um). Sections were washed 1x in TBST, followed by one wash in 0.1% Tris-HCL pH 8.5. The VectorRed Alkaline phosphatase substrate staining solution (Vector Laboratories Cat# SK-5100) was prepared following the manufacturer's instruction in 0.1M Tris-HCL pH 8.5. Brain sections were incubated in the AP staining solution for 30 minutes at room temperature, followed by 3 washes in Tris-HCL pH 8.5. Sections were mounted on Superfrost Plus microscopy slides, air-dried overnight, cleared in Xylene and coverslipped with Permount. Sections treated with the selective TNAP inhibitor SBI-425 were used as a control to assess the specificity of the AP activity labelling. Images of the hippocampal dentate gyrus region were acquired on a Zeiss Epifluorescent microscope or Keyence bright-field microscopy for 3-5 hippocampal sections per mouse and quantified using FIJI. For co-labeling experiments, brain sections were first labelled for AP-activity staining, followed by standard immunohistochemistry for CD31/AQP4 as outlined in the immunohistochemistry section.

Thioflavin S labelling

Sections were rinsed three times in PBS, mounted on Superfrost Plus slides and air dried overnight.[69] The sections were then incubated in freshly prepared and filtered 0.1% thioflavin S (ThioS) solution in 20% ethanol for 30 min at room temperature. The samples were rinsed twice with 20% ethanol for 2 min, followed by 2 washes in water. Following the Thioflavin S staining, sections were treated with 1:100 dilution of TrueBlack (Biotium cat# 23007) in 70% ethanol for 2 minutes and coverslipped with Prolong Gold. Images of the hippocampal dentate gyrus region were acquired on a Zeiss LSM800 or LSM900 confocal microscope and quantified using FIJI. On representative images, ThioS was detected in both the blue and green channels and appears as a merge on the representative images. The thresholded area occupied by the ThioS labelling in the dentate gyrus region of the hippocampus was quantified and averaged for 3-5 hippocampal sections per mouse.

TNAP cleavage assay

A lentiviral Alpl/TNAP expression plasmid was first cloned under the control of the CMV promoter. Lentiviral particles were generated by co-transfecting HEK293T cells with the lentiviral Alpl/TNAP expression plasmid and lentiviral packaging plasmids

Please cite this article in press as: Bieri et al., Liver exerkine reverses aging- and Alzheimer's-related memory loss via vasculature, Cell (2026), https://doi.org/10.1016/j.cell.2026.01.024

(Addgene Plasmids# 12259 and 12260 were gifts from Didier Trono) using Lipofeamine 3000 (ThermoFisher, Cat# L300015).[70] Viral solution was collected 48 hours after transfection using 10 minute centrifugation at 1000g. The supernatant was collected and lentiviral particles purified and concentrated using 90 minute ultracentrifugation at 24'000 RPM (Beckman Coulter). TNAP reporter cells were generated by infecting HEK293T cells with the lentiviral particles, followed by subcloning and testing individual colonies. TNAP expression in reporter cells was validated using Western blot analysis. Reporter cells were plated at a confluency of 75-90% for transfection experiments and cultured in DMEM + 10% FBS. Lipofectamine 3000 was used as the transfection reagent. The TNAP reporter cells were transfected with GFP, mouse and human GPLD1, or enzymatically inactive mouse H133N GPLD1 expression constructs. The supernatant was collected at 48 hours for downstream analysis. A SEAP reporter assay kit (Abcam, Cat# 133077) was used to measure alkaline phosphatase activity in the media. Cells treated with the TNAP inhibitor SBI-425 (1uM) were used as a negative baseline control.

QUANTIFICATION AND STATISTICAL ANALYSIS

Data, statistical analyses, and reproducibility

All experiments were randomized and blinded by an independent researcher. Researchers remained blinded throughout histological, biochemical and behavioral assessments. Groups were unblinded at the end of each experiment on statistical analysis. Data are expressed as mean ± s.e.m. The distribution of data in each set of experiments was tested for normality using the D'Agostino–Pearson omnibus test or Shapiro-Wilk test. Statistical analysis was performed using Prism 8-10 (GraphPad). Means between two groups were compared using two-tailed unpaired Student's *t* tests. Comparisons of means from multiple groups with each other were analyzed using one-way ANOVA followed by the appropriate post hoc test, as indicated in the figure legends. Additional statistical details are indicated in the respective figure legends. All data generated or analyzed in this study are included in this article.

CellPress
OPEN ACCESS

Supplemental figures

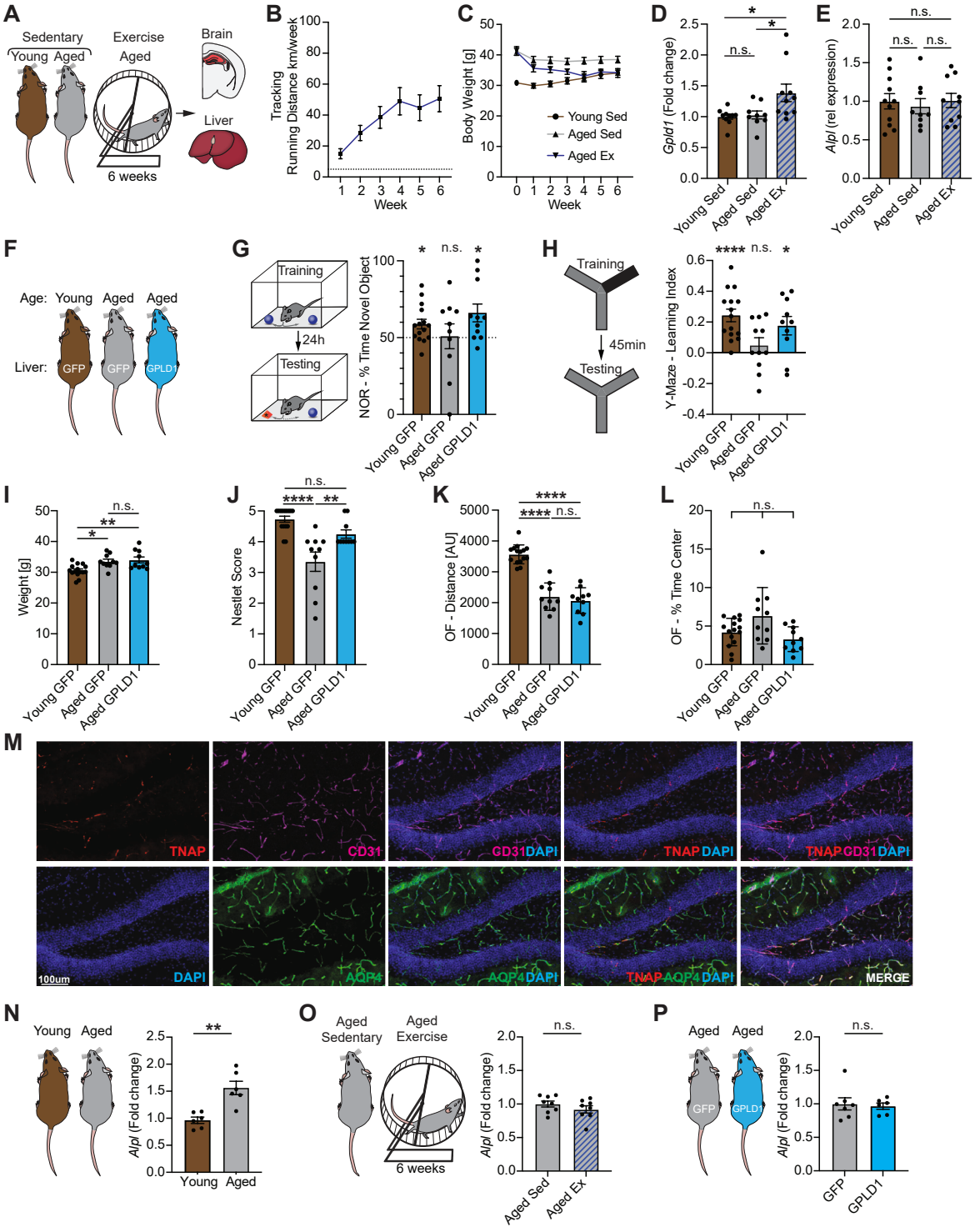

(legend on next page)

Figure S1. Increasing liver-derived GPLD1 rejuvenates cognition and health metrics in aged mice, related to Figure 1

(A) 6-week voluntary exercise intervention in aged (19–21 months) mice. Sedentary young (3–4 months) and aged mice were used as controls to assess age-related changes.

(B) Weekly running distance (kilometers, km) for aged exercise mice (average of n = 10 mice/group).

(C) Weekly body weight measurements for young and aged control mice and aged exercise mice (n = 8–10 mice/group).

(D) Liver *Gpld1* gene expression as measured by RT-qPCR analysis (n = 8–10 mice/group).

(E) Liver *Alpl* (TNAP) gene expression as measured by RT-qPCR analysis (n = 8–10 mice/group).

(F) Schematic illustrating experimental groups of young (3–4 months) and aged mice (19–21 months) with liver expression of GPLD1 or GFP control using an HDTVI delivery approach. Animals were behaviorally tested 30 days post treatment.

(G) Object recognition memory was assessed using NOR and quantified as percent time spent exploring a novel versus familiar object (n = 10–15 mice/group).

(H) Spatial working memory was measured in the Y-maze task as the discrimination index for the novel arm (n = 10–15 mice/group).

(I) Body weight measurements (n = 10–15 mice/group).

(J) Hippocampal-dependent nest-forming performance was scored from 1 (worst) to 5 (best) (n = 10–15 mice/group).

(K and L) Activity (K, total distance) and anxiety (L, % time in center) were assessed using the open field (OF) assay, during which mice explored an empty arena for 10 min (n = 10–15 mice/group).

(M) Representative images of TNAP (red), CD31 (magenta), AQP4 (green), and DAPI labeling in the DG region of the hippocampus. Complementary images to the aged group in Figure 1D.

(N) Hippocampal *Alpl* gene expression as measured by RT-qPCR analysis in young (3 months) and aged (22–24 months) mice (n = 6 mice/group).

(O) Hippocampal *Alpl* gene expression in aged exercised and sedentary mice (21–22 months) as measured by RT-qPCR analysis (n = 8 mice/group).

(P) Hippocampal *Alpl* gene expression in aged mice (20–22 months) following liver overexpression of GPLD1 or GFP control using an HDTVI delivery approach, as measured by RT-qPCR analysis (n = 5–7 mice/group).

Data shown as mean ± SEM. Statistical analysis was performed using ANOVA with Šidák's post hoc (D, E, and I–L), one-sample t test versus 50% (G) or 0 (H), and t test (N–P); $^{*}p < 0.05$, $^{**}p < 0.01$, $^{****}p < 0.0001$.

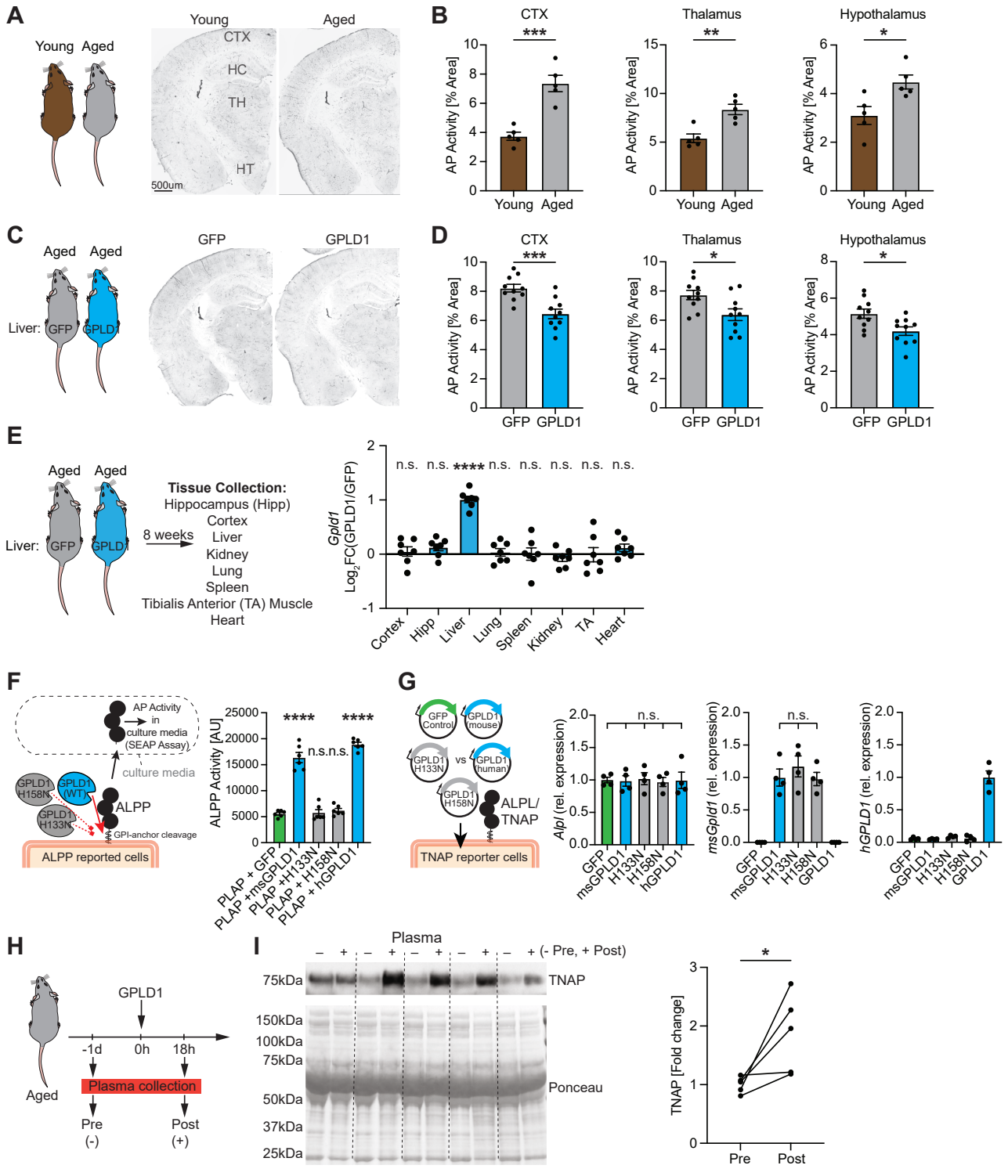

Figure S2. Characterization of TNAP/ALPL expression and cleavage across different ages, interventions, and tissues, related to Figure 1

(A) Alkaline phosphatase (AP) activity measurements in young (3–4 months) and aged (22–24 months) mice. Representative images of endogenous AP labeling in the brains from young and aged mice. Cortex (CTX), hippocampus (HC), thalamus (TH), and hypothalamus (HT) regions labeled on a representative brain section (stitched overview image).

(B) Quantification of AP labeling in the cortex, thalamus, and hypothalamus of young and aged mice (n = 5 mice/group).

(legend continued on next page)

(C) Representative endogenous AP labeling in the brain of aged mice (20–22 months) following liver overexpression of GPLD1 or GFP control (stitched overview image).
(D) Quantification of AP labeling in the cortex, thalamus, and hypothalamus of aged GPLD1-treated mice (n = 10 mice/group).
(E) Expression analysis in aged mice (21–22 months) with liver expression of GPLD1 or GFP control using an AAV-mediated overexpression approach. Tissues were collected 8 weeks after AAV delivery, and *Gpld1* gene expression was measured by RT-qPCR analysis, represented as a fold change from the GFP control group for each tissue (n = 6–7 mice/group).
(F) Schematic illustration (left) and quantification (right) of GPLD1 cleavage activity using the Placental AP (ALPP)-based reporter assay. ALPP reporter cells are treated with expression constructs for WT mouse (ms) and human (h) GPLD1, catalytically inactive GPLD1 with the H133N amino acid substitution (H133N) or H158 amino acid substitution (H158N), or GFP control. AP activity is measured in the cell culture media upon GPLD1 cleavage of ALPP.
(G) Schematic illustration of TNAP reporter cells treated with expression constructs for msGPLD1, hGPLD1, catalytically inactive H133N and H158N GPLD1, or GFP control. *Alpl*, mouse *Gpld1*, and human *GPLD1* gene expression as measured by RT-qPCR analysis in TNAP reporter cells (n = 4 wells/condition). n/d indicates no detectable gene expression.
(H) *In vivo* TNAP cleavage paradigm. Aged mice (22–24 months) with liver GPLD1 overexpression using an HDTVI approach. Baseline (−pre) and treatment plasma (+post) were collected prior to and 18 h after HDTVI.
(I) Representative western blot and quantification of TNAP in plasma of GPLD1-treated mice (n = 5 mice).
Data shown as mean ± SEM. Statistical analysis was performed using t test (B and D), one-sample t test versus 0 (E), ANOVA with Šidák's post hoc test (F and G), and paired t test (I); $^{*}p < 0.05$, $^{**}p < 0.01$, $^{***}p < 0.001$, $^{****}p < 0.0001$.

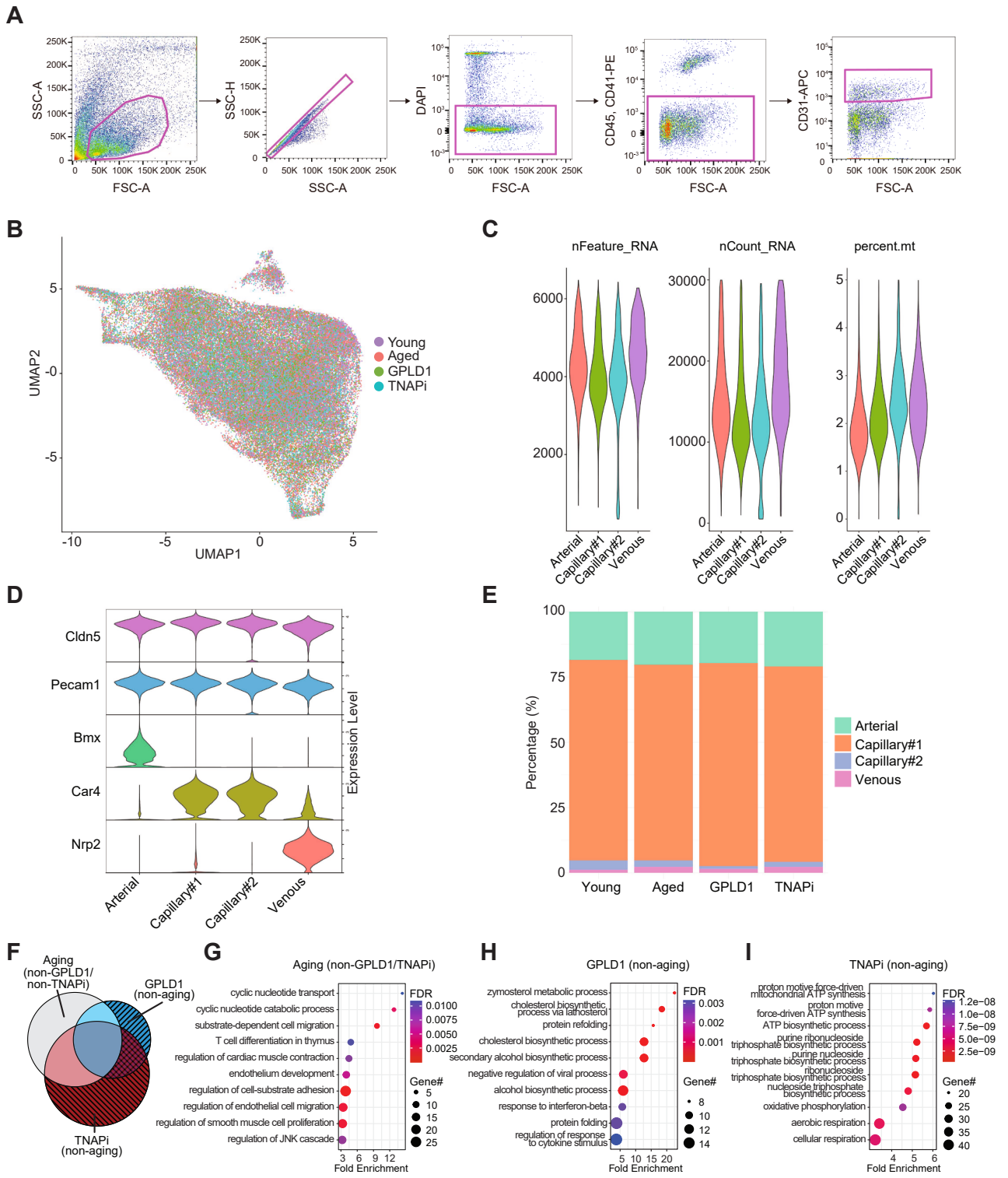

Figure S3. Isolation and scRNA-seq gene signatures of BECs from young, aged, GPLD1-, and TNAPi-treated aged mice, related to Figures 2 and 5

(A) Fluorescence-activated cell sorting gating strategy for CD31-expressing BECs.

(B) Cell origin based on age and treatment group overlaid on UMAP of hippocampal BECs.

(C) Violin plots of quality metrics including number counts (left), number of unique features (middle), and percent mitochondrial RNA (right) by cell cluster.

(legend continued on next page)

(D) Violin plots of representative genes for each cell type identified via scRNA-seq of hippocampi from aged mice with liver expression of GPLD1 or catalytically inactive H133N-control (CTRL) or aged mice treated with a TNAP inhibitor (TNAPi).
(E) Bar graph visualizing the proportion of captured cell types by age and treatment group.
(F) Venn diagram showing the overlap of DEGs among BEC aging, GPLD1 treatment, and TNAPi.
(G) Top GO biological process terms selectively enriched in DEGs associated with BEC aging, independent of GPLD1 or TNAPi effects.
(H) Top GO biological process terms enriched in DEGs for the GPLD1 comparison independent of aging.
(I) Top GO biological process terms enriched in DEGs for the TNAPi comparison independent of aging.

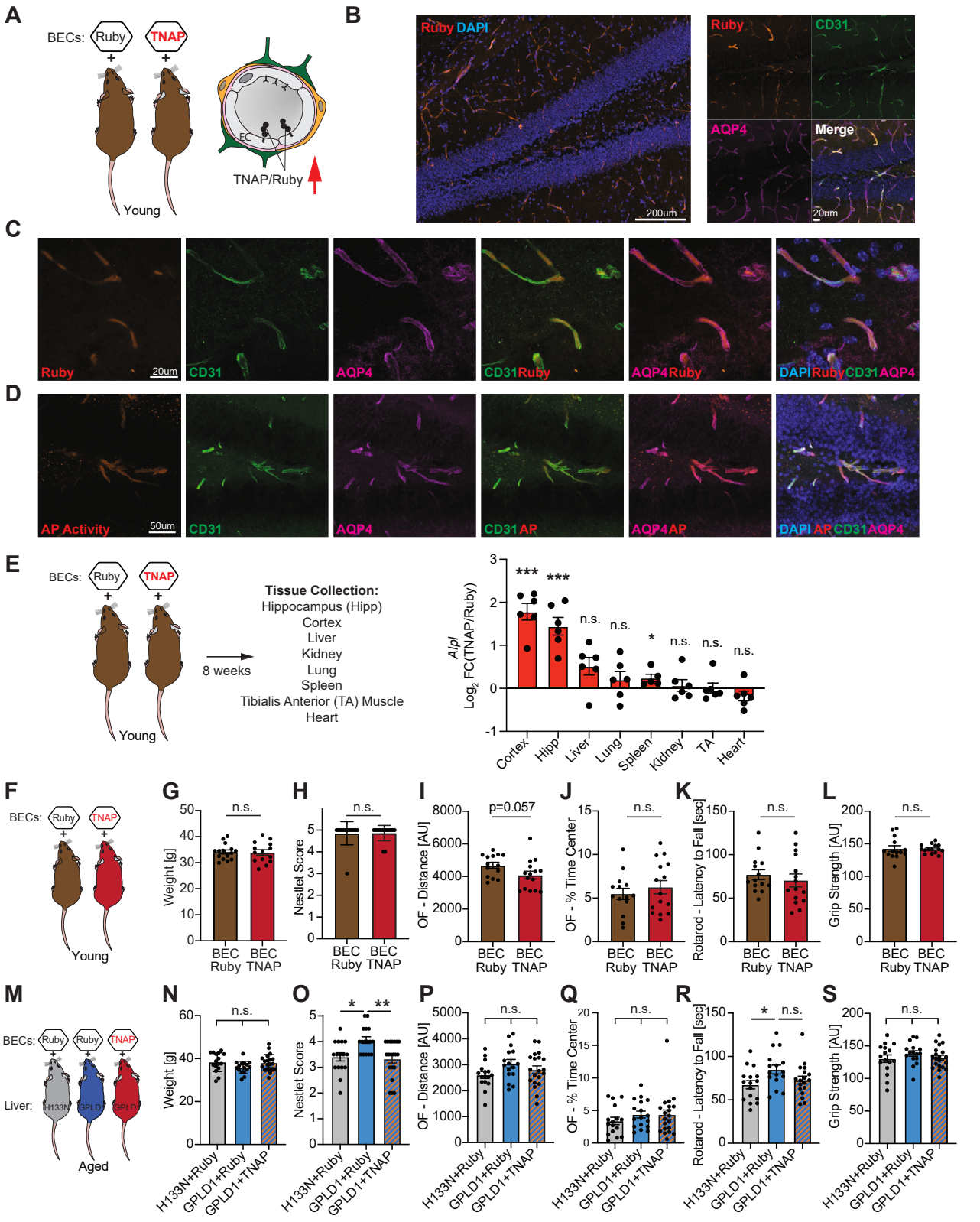

(legend on next page)

Figure S4. Expression analysis and assessment of health metrics in mice following BEC expression of TNAP, related to Figures 3 and 4

(A) Young mice (3–4 months) were injected with AAVs to increase the expression and activity of the GPI-anchored protein TNAP in BECs. After 6–8 weeks, mice underwent gene expression and behavioral analyses.

(B) Representative images showing the expression of the control virus encoding the red fluorescent protein mRuby2 (Ruby), delivered using the PHP.V1 AAV capsid, which preferentially targets BECs. Co-immunolabeling of Ruby (red) with the endothelial and vascular marker CD31 (green) and end-feet marker AQP4 (magenta) in the DG region of the hippocampus.

(C) Representative high-magnification confocal images of Ruby and vascular markers CD31 and AQP4 in the DG region of the hippocampus.

(D) Representative confocal image of alkaline phosphatase (AP) labeling (red) with the vascular markers CD31 (green) and AQP4 (magenta) in the DG.

(E) A series of tissues was isolated from young (3–4 months) mice 8 weeks after AAV-mediated overexpression of TNAP or Ruby. Tissue *Alpl* gene expression as measured by RT-qPCR analysis (n = 8–10 mice/group), represented as a fold change from the Ruby control group (n = 6 mice/group).

(F) Behavioral and health metrics assessment in young (3–4 months) mice with TNAP overexpression in BECs.

(G) Body weight measurements (n = 14–15 mice/group).

(H) Hippocampal-dependent nest-forming performance was scored from 1 (worst) to 5 (best) (n = 14–15 mice/group).

(I and J) Activity (I, total distance) and anxiety (J, % time in center) were assessed using the open field (OF) assay, during which mice explored an empty arena for 10 min (n = 14–15 mice/group).

(K) Motor coordination was assessed using the RotaRod assay as the latency to fall from an accelerating rotating cylinder (n = 14–15 mice/group).

(L) 4-paw grip strength was measured using a standard grip strength apparatus with a wire grid (n = 14–15 mice/group).

(M) Behavioral and health metrics assessment in aged (22–24 months) mice with liver-specific expression of GPLD1 or catalytically inactive H133N-GPLD1 and BEC-specific overexpression of TNAP or Ruby control.

(N) Body weight measurements.

(O) Nest-forming performance.

(P and Q) Activity (P, total distance) and anxiety (Q, % time in center) were assessed using the OF assay (n = 16–20 mice/group).

(R) Motor coordination was assessed using the RotaRod assay as the latency to fall from an accelerating rotating cylinder.

(S) 4-paw grip strength (n = 16–20 mice/group).

Data shown as mean ± SEM. Statistical analysis was performed using a one-sample t test versus 0 (F), t test (G–L), and ANOVA with Šidák's post hoc test (N–S); $^{*}p < 0.05$, $^{**}p < 0.01$, $^{***}p < 0.001$.

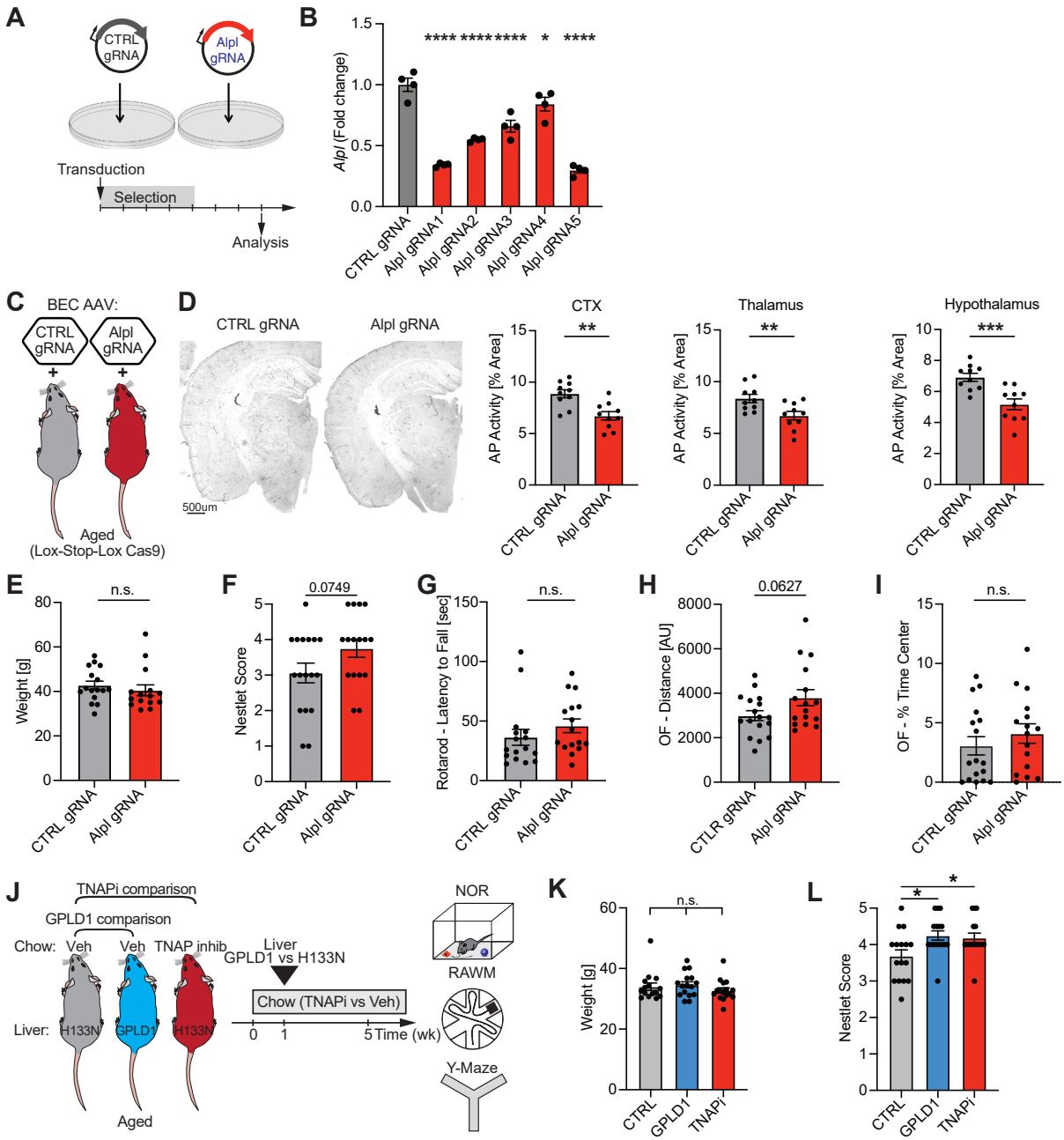

(legend on next page)

Figure S5. Assessment of health metrics following viral-mediated cerebrovascular TNAP abrogation or TNAP inhibition in aged mice, related to Figure 4

(A) gRNA testing in mouse Neuro2a cells 7 days after transduction with viral particles expressing Cas9, Alpl-targeting gRNAs, and a puromycin selection cassette.
(B) *Alpl* gene expression as measured by RT-qPCR analysis, represented as a fold change from the non-targeting control gRNA control condition (n = 4 wells/condition).
(C) Aged (20–22 months) Cas9 mice with an inducible Lox-stop-Lox Cas9 cassette, administered with BEC-targeting AAVs (PhP.V1 capsid) expressing Cre and gRNAs to selectively abrogate cerebrovascular TNAP.
(D) Representative images of whole coronal brain sections with endogenous alkaline phosphatase (AP) labeling in the brain of aged Cas9 mice 5–8 weeks after ablation of BEC-TNAP. Quantification of AP labeling in the cortex, thalamus, and hypothalamus (n = 10 mice/group).
(E) Body weight measurements.
(F) Hippocampal-dependent nest-forming performance was scored from 1 (worst) to 5 (best).
(G) Motor coordination was assessed using the RotaRod assay as the latency to fall from an accelerating rotating cylinder.
(H and I) Activity (H, total distance) and anxiety (I, % time in center) were assessed using the OF assay, during which mice explored an empty arena for 10 min (n = 15–17 mice/group).
(J) Aged mice (22–24 months) with liver overexpression of GPLD1, inactive H133N GPLD1, or systemic TNAP inhibition (TNAPi) via SBI-425 administration in specialized chow.
(K) Body weight measurements.
(L) Nest-forming performance.
(M) Motor coordination assessed using RotaRod testing.
(N) 4-paw grip strength.
(O and P) Activity (O, total distance) and anxiety (P, % time in center) were assessed using OF testing (n = 15–17 mice/group).
Data shown as mean ± SEM. Statistical analysis was performed using ANOVA with Šidák's post hoc test (B and K–P) and t test (D–I); $^{*}p < 0.05$, $^{**}p < 0.01$, $^{***}p < 0.001$, $^{****}p < 0.0001$.

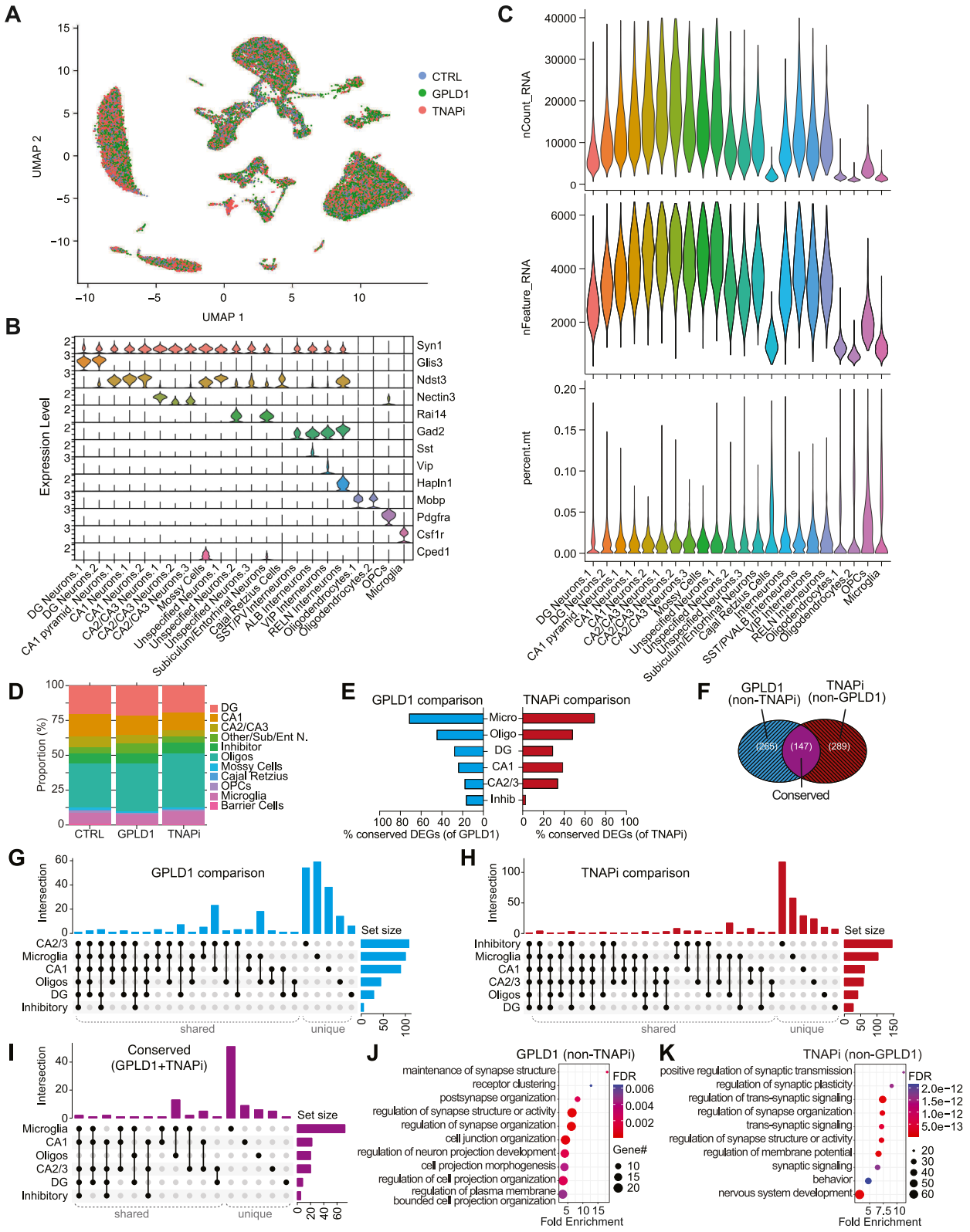

(legend on next page)

Figure S6. snRNA-seq gene signatures and gene expression changes in GPLD1- and TNAPi-treated aged mice, related to Figure 5

(A) Cell origin based on age and treatment group overlaid on UMAP of hippocampal nuclei.

(B) Violin plots of representative genes for each cell type identified via snRNA-seq of hippocampi from aged mice with liver expression of GPLD1 or catalytically inactive H133N-control (CTRL) or aged mice treated with a TNAP inhibitor (TNAPi).

(C) Violin plots of quality metrics, including number counts (top), number of unique features (middle), and percent mitochondrial RNA by cell cluster.

(D) Bar graph visualizing the proportion of captured cell types by treatment group. Dentate gyrus (DG) neurons; OPCs, oligodendrocyte progenitor cells; oligos, oligodendrocytes.

(E) Bar graph representing the percentage of conserved DEGs by cell type between the GPLD1 comparison and the TNAPi comparison. The left bars (blue) are normalized to the GPLD1 comparison, and the right bars (red) are normalized to the TNAPi comparison.

(F) Venn diagram showing unique and overlapping DEGs for the GPLD1 and TNAPi comparisons.

(G) UpSet plot displaying shared and unique DEGs per cell type for the GPLD1 comparison.

(H) UpSet plot displaying shared and unique DEGs per cell type for the TNAPi comparison.

(I) UpSet plot displaying shared and unique conserved DEGs between both GPLD1 and TNAPi comparisons, by cell type.

(J) Top GO biological process terms selectively enriched in DEGs associated with the GPLD1 comparison independent of TNAPi effects.

(K) Top GO biological process terms selectively enriched in DEGs associated with the TNAPi comparison independent of GPLD1 effects.

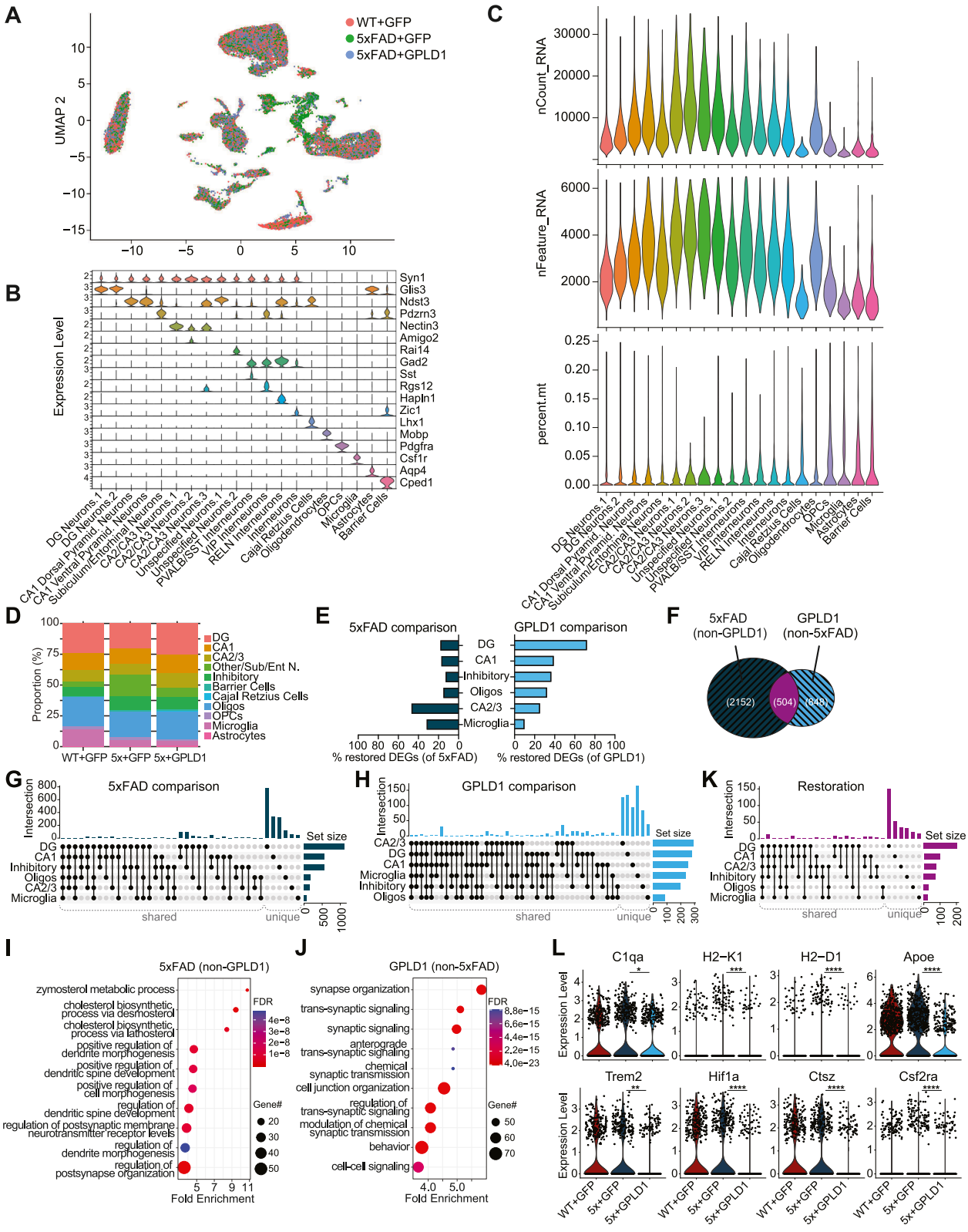

(legend on next page)

Figure S7. snRNA-seq gene signatures and gene expression changes in GPLD1-treated 5xFAD mice, related to Figure 6

(A) Cell origin based on age and treatment group overlaid on UMAP of hippocampal nuclei.

(B) Violin plots of representative genes for each cell type identified via snRNA-seq of hippocampi from 5xFAD or WT littermates with liver expression of GPLD1 or GFP control.

(C) Violin plots of quality metrics, including number counts (top), number of unique features (middle), and percent mitochondrial RNA by cell cluster.

(D) Bar graph visualizing the proportion of captured cell types by treatment group. Dentate gyrus (DG) neurons; OPCs, oligodendrocyte progenitor cells; oligos, oligodendrocytes.

(E) Bar graph representing the percentage of conserved DEGs by cell type between the 5xFAD comparison and the GPLD1 comparison. The left bars (navy) are normalized to the 5xFAD comparison, and the right bars (light blue) are normalized to the GPLD1 comparison.

(F) Venn diagram showing unique and overlapping DEGs for the 5xFAD and GPLD1 comparisons.

(G) UpSet plot displaying shared and unique DEGs per cell type for the 5xFAD (5xFAD GFP versus WT GFP) comparison.

(H) UpSet plot displaying shared and unique DEGs per cell type for the 5xFAD GPLD1 comparison.

(I) Top GO biological process terms selectively enriched in DEGs associated with the 5xFAD comparison independent of GPLD1 effects.

(J) Top GO biological process terms selectively enriched in DEGs associated with the GPLD1 comparison independent of 5xFAD effects.

(K) UpSet plot displaying shared and unique restored DEGs between both 5xFAD and GPLD1 comparisons by cell type.

(L) Violin plots of disease-associated microglia (DAM)-related and inflammatory genes in the microglia cluster.

Statistical analysis was performed using MAST differential gene expression analysis between the 5xFAD control and the GPLD1 condition (L); $^{*}p < 0.05$, $^{**}p < 0.01$, $^{***}p < 0.001$, $^{****}p < 0.0001$.

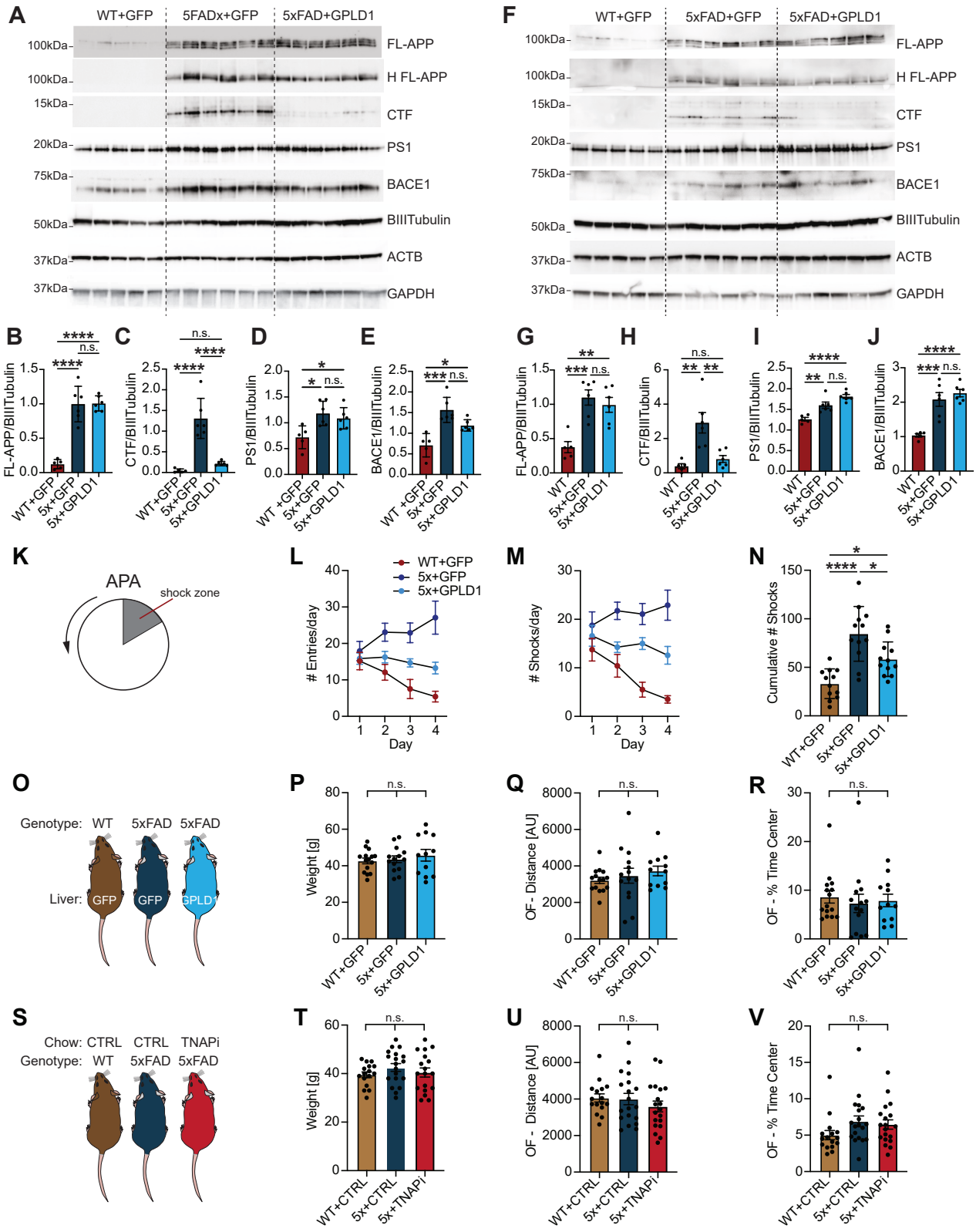

(legend on next page)

Figure S8. Assessment of APP processing and health metrics in GPLD1-treated 5xFAD mice, related to Figure 7

(A) Representative immunoblots of hippocampal lysates from WT mice and 5xFAD littermates with liver expression of GPLD1 or GFP control. Human and mouse full-length APP (H FL-APP and FL-APP), human APP C-terminal fragments (CTF), and APP processing proteins Beta-secretase 1 (BACE1) and Presenilin 1 (PS1) were assessed. BIIITubulin, GAPDH, and actin beta (ACTB) were used as loading controls.

(B and C) Quantification of full-length APP (B) and CTF (C).

(D and E) Quantification of APP processing proteins PS1 (D) and BACE1 (E) (n = 5–6 mice/group).

(F) Representative immunoblots of cortical lysates from WT mice and 5xFAD littermates with liver expression of GPLD1 or GFP control. Human and mouse full-length APP, human APP CTF, and APP processing proteins BACE1 and PS1 were assessed. BIIITubulin, GAPDH, and ACTB were used as loading controls.

(G and H) Quantification of FL-APP (G) and CTF (H).

(I and J) Quantification of APP processing proteins PS1 (I) and BACE1 (J) (n = 5–6 mice/group).

(K) Active place avoidance (APA) paradigm—mice have to learn to avoid a stationary 60° area (shock zone) using visual cues placed around the arena. APA was tested 10–12 weeks after AAV-mediated overexpression of GPLD1 or GFP control in the livers of adult 5xFAD mice (8–9 months).

(L–N) Measurement of daily shock zone entries (L), number of delivered foot shocks per day (M), and cumulative number of foot shocks over the duration of 4 days of tasting (N) (n = 12 mice/group).

(O) Health metrics measurements in 5xFAD mice (9–10 months) with liver GPLD1 or GFP control overexpression using the HDTVI approach.

(P) Body weight measurements.

(Q and R) Activity (Q, total distance) and anxiety (R, % time in center) were assessed using the OF assay, during which mice explored an empty arena for 10 min (n = 12–15 mice/group).

(S) Health metrics measurements in mature 5xFAD mice (11–12 months) following systemic TNAP inhibition (TNAPi) via SBI-425 administration (11–12 weeks) in specialized chow.

(T) Body weight measurements.

(U and V) Activity (U, total distance) and anxiety (V, % time in center) assessed using OF testing (n = 17–20 mice/group).

Data shown as mean ± SEM. Statistical analysis was performed using ANOVA with Šidák's post hoc test (B–E, G–J, N, P–R, and T–V); $^{*}p < 0.05$, $^{**}p < 0.01$, $^{***}p < 0.001$, $^{****}p < 0.0001$.